

Final Report

Contract # Number:

W911NF-07-2-0072

Program Title:

Advanced Bonded Diamond for Optical Applications

Prime Contractor:

Onyx Optics, Inc.

6551 Sierra Lane

Dublin, Ca 94568

www.onyxoptycs.com



Program Manager:

Helmuth Meissner

Onyx Optics, Inc.

6551 Sierra Lane

Dublin, CA 94568

Email: hmeissner@onyxoptycs.com

Ph: 925-833-1969

Fax: 925-833-1759

Document Preparation Date: 11/28/2011

20111129050



DEFENSE TECHNICAL INFORMATION CENTER

Information for the Defense Community

DTIC® has determined on 12/28/11 that this Technical Document has the Distribution Statement checked below. The current distribution for this document can be found in the DTIC® Technical Report Database.

☒ **DISTRIBUTION STATEMENT A.** Approved for public release; distribution is unlimited.

☐ **© COPYRIGHTED.** U.S. Government or Federal Rights License. All other rights and uses except those permitted by copyright law are reserved by the copyright owner.

☐ **DISTRIBUTION STATEMENT B.** Distribution authorized to U.S. Government agencies only (fill in reason) (date of determination). Other requests for this document shall be referred to (insert controlling DoD office).

☐ **DISTRIBUTION STATEMENT C.** Distribution authorized to U.S. Government Agencies and their contractors (fill in reason) (date determination). Other requests for this document shall be referred to (insert controlling DoD office).

☐ **DISTRIBUTION STATEMENT D.** Distribution authorized to the Department of Defense and U.S. DoD contractors only (fill in reason) (date of determination). Other requests shall be referred to (insert controlling DoD office).

☐ **DISTRIBUTION STATEMENT E.** Distribution authorized to DoD Components only (fill in reason) (date of determination). Other requests shall be referred to (insert controlling DoD office).

☐ **DISTRIBUTION STATEMENT F.** Further dissemination only as directed by (insert controlling DoD office) (date of determination) or higher DoD authority.

Distribution Statement F is also used when a document does not contain a distribution statement and no distribution statement can be determined.

☐ **DISTRIBUTION STATEMENT X.** Distribution authorized to U.S. Government Agencies and private individuals or enterprises eligible to obtain export-controlled technical data in accordance with DoDD 5230.25; (date of determination). DoD Controlling Office is (insert controlling DoD office).

1. Diamond growth research with Chemical Vapor Deposition (CVD) technology

1.1 Optimization of the Biasing Enhanced Nucleation (BEN) configuration for Highly Oriented Diamond (HOD) growth

The customized CVD reactor has been successfully running for over 2 years. Some encouraging results have been achieved on it. Two important features of the reactor proved crucial, which are a motorized cooling stage and DC-biasing ability. The core component of the DC-biasing function is a ring shaped molybdenum (Moly) piece resting on a quartz cylinder. The Moly ring is electrically insulated from the stage, and can be DC biased to several hundreds of Volts. Because the Moly ring has contact with the chamber plasma, the plasma will be biased as a result. Therefore, the active carbon molecules inside the plasma will be accelerated and bombarded to the silicon substrate, which results in effective diamond seeding under certain conditions. This seeding method is called Biasing Enhanced Nucleation (BEN).

1.1.1 Review of current bias ring structure

As shown in figure 1, current biasing design features an electrically insulated Moly ring sitting on a quartz cylinder. The Moly ring is connected with a nickel wire using a nickel screw nut. The nickel wire is inserted through the hole on the stage, and is carefully insulated with kapton tape. While this design successfully realized BEN, disadvantages have been identified after several years' use. Among them, the most serious disadvantage is the catalytic effect of the exposed nickel nut in the carbon rich chamber environment. As a result, considerable graphite condensation will happen on it after each run. Such graphite condensation will be a contamination source for the diamond deposition. The situation becomes unacceptable for a long time growth. Another disadvantage lies in the distortion of the microwave mode inside the chamber. It is well known that the microwave mode inside the chamber is very sensitive to any physical obtrusions. The small nickel nut sticking out from the smooth Moly ring will distort the initial symmetric microwave mode. And such mode distortion will lead to poor diamond uniformity after long time growth.

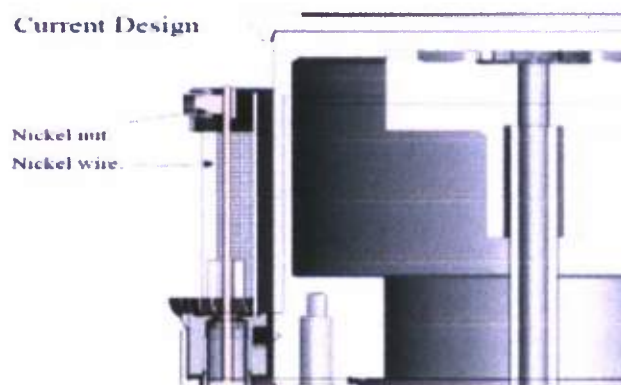


Figure 1. Current biasing ring structure

1.1.2 Redesigns of the bias ring structure

Based on the above observations, new designs have been suggested, whose pros and cons are listed below. Illustrated in figure 2-a, the first redesign features a Moly ring of thinner geometric size and a revised contact mechanism of pin/socket method. The thinner size of the ring will disrupt to a lesser degree the phi-symmetry of the electric field, and the new contact mechanism will simplify the ring installation and service. The wire used can be either tungsten or Moly. The disadvantage of such design is that the bias ring is still exposed to the plasma during long time growth, when it is not needed.

Illustrated in figure 2-b, the redesign-II of the bias ring structure shares the similar contact mechanism with the redesign-I. However, the quartz insulator has been shortened in favor of a Moly cylinder on the top. This thin Moly cylinder will sit on the grooved Moly ring by gravity. Such structure first can promote or enforce a greater degree of phi-symmetry. The top Moly cylinder can be readily removed during long time growth. In this way, unnecessary direct contact between the plasma and the bias ring can be avoided.

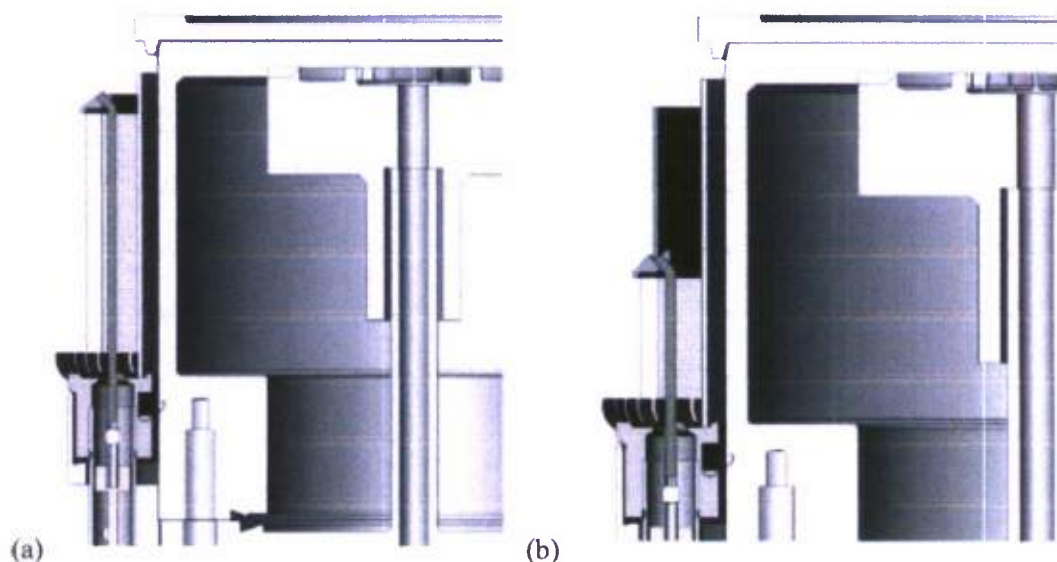


Figure 2. Redesign-I of the bias ring structure

Shown in figure 3-a, the redesign-II features a simplified (straight, vertical) metal wire (tungsten or Moly) as electrode connector. The design requires press fit into the flat-top Moly ring, and it also requires pin/socket choke. The advantages of such design are simplicity and lower vertical profile to ring. And the con lies in the reduced distance between ring and central parts, where the chance for arcing will increase. Another disadvantage of such design is that the bias ring is still exposed to the plasma during long time growth.

The revised design is demonstrated in figure3-b, which has an additional part, an outer Moly tube. Besides easy removal of the Moly cylinder during the long time run, the intent is also to use a larger, phi-symmetric part to move the asymmetric connection point lower, and thereby improve circular uniformity of deposition.

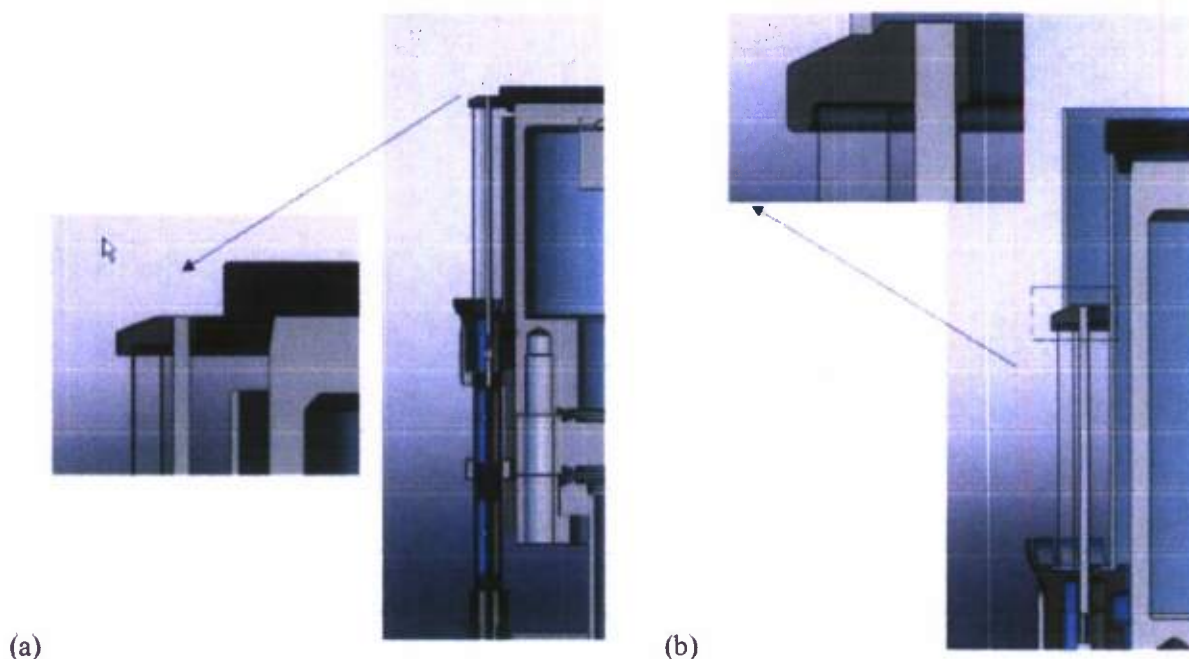


Figure 3. Redesign-II of the bias ring structure.

As a conclusion, the idea of adding a Moly cylinder on the top of bias ring has the advantage of easy exchange and less interference to the microwave cavity. The comparison between the two suggested wire connection mechanisms will be performed next.

1.2 Development of the oxygen related recipe for HOD diamond film growth

Traditionally, films with square $\{100\}$ can be formed in two basic ways. The first way is to operate with α near 1. This will produce the square shapes during the initial stages of growth when the film thickness is only on the order of the initial spacing between the nucleation seeds. Specifically, randomly oriented seed crystals will grow into small cube shapes with $\alpha = 1$. Continued growth under low secondary nucleation conditions will form a $\langle 111 \rangle$ texture because this direction grows fastest. Another way to form square facets is to grow a thick film with a $\langle 100 \rangle$ texture. This is done with α less or equal 3. As the film grows thick, the texture forms and the $[100]$ directions are perpendicular to the substrate surface. The value of α slightly less than 3 (e.g. 2, 2.5) leads to the square tops on the crystals in the film. These square facets are well aligned parallel to the surface of the growing film. This is the growth condition that leads to smooth coplanar (100) faceted thick polycrystalline diamond films.

Once the α parameter can be mapped, two-step processes will be developed that use $\alpha = 3$ or near 3 to grow highly $\langle 100 \rangle$ textured films during the initial growth phase. Then for the second growth phase the growth conditions are changed so that the α parameter is reduced in value. This increases the relative growth rate of the $[111]$ direction to the $[100]$ direction and the film growth fills the valleys located between the (100) faces present in the first phase. The resultant film has a top surface covered with (100) facets parallel with the substrate surface.

Another factor that influences the surface morphology is the extent and influence of twinning that can occur. It was found that the α parameter also influences the formation and effect of twinning. When $\alpha > 2$, the {100} facets are stable with respect to twinning. Stable means that if a small twin occurs on a {100} facet it will disappear as film growth continues. The other stability condition is that for $\alpha < 1.5$ the {111} facets are stable with respect to twins.

Based on the above technical route, especially with the N_2 addition in the recipe, free standing HOD film has been successfully achieved. However, the quality of the obtained HOD sample was seriously limited by the high density of grain boundaries. In searching for a N_2 -free growth recipe, oxygen addition gives an effective way to improve the HOD optical quality. The addition of oxygen to the input gas flow, either as O_2 , CO , or CO_2 , can be useful for optical quality diamond deposition. Generally, excess oxygen will etch the carbon from the surface, preventing diamond growth, and any excessive carbon in large amounts will lead to the deposition of non-diamond carbon films.

The result of oxygen addition usually is larger diamond grain sizes and less SP_2 material in the film. The oxygen reduces SP_2 incorporation in the film and also reduces secondary nucleation, which leads to larger crystals and altered surface morphology. This is believed to occur because of the increased etching effect of oxygen radicals. The addition of small amount of oxygen may improve the growth rate, while too much oxygen addition will reduce the growth rate as etching effect becomes significant. In some cases, it leads to lower deposition temperatures 100-150C without a loss of growth rate. On the other hand, the introduction of oxygen into the feed gas will influence the α parameter. Typically, higher oxygen will give larger α parameter. Similar effects can be observed when increasing the carbon percentage or reducing the temperature.

1.2.1 Oxygen addition recipe after BEN

Diamond growth using only oxygen addition after BEN has been investigated. The result shows a high percentage of non-(100) growth as shown in figure 4a. The typical growth condition was 1050C, 0.25% O_2 , 400scm total flow, 2% CH_4 . The diamond quality was good according to the Raman spectrum.

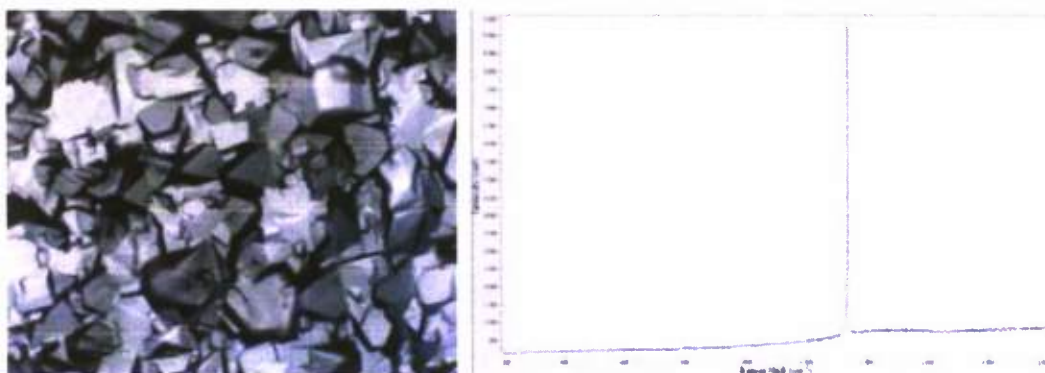


Figure 4a. Oxygen recipe growth after BEN seeding. Left: surface morphology, Right: Raman spectrum

Growth under the same condition on HOD substrate gives a much better result. The oxygen addition was also investigated from small amount, 0.1%, to large amount, 1%, of the total gas flow. Its effects are shown in figure 4b. First, twin density drops significantly when increasing oxygen addition. Second, higher oxygen addition leads to pyramid like surface profile, which indicates a larger α parameter.

This phenomenon is consistent with the previous conclusion. The optimal oxygen percentage was found to be around 0.25% of the total flow. As we can see from the figure, the (100) diamond grains are merging together with limited grain boundary formation.

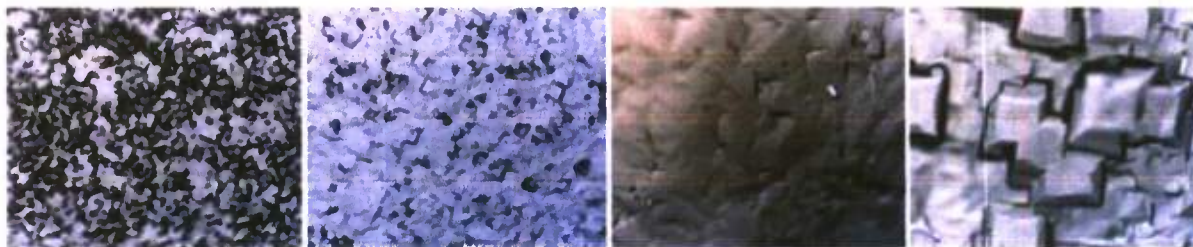


Figure 4b. Effects of oxygen addition (left to right with increasing oxygen amount)

It is also noticed that the film quality of the after-growth has strong relation with initial HOD quality. The existing surface defects on the initial HOD film are difficult to remove after growth with the above oxygen recipe. This is shown in figure 5, which compares the growth cases of different initial HOD quality.

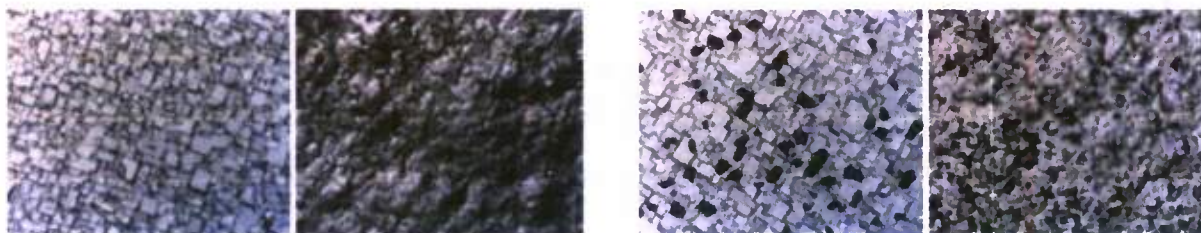


Figure 5. Initial HOD quality is important in achieving good surface finish. Left (good) and right (bad).

The above oxygen recipe has been tested on HOD substrate for 20h with satisfactory surface morphology, even though the growth rate is as low as $2\mu\text{m/h}$. However, this oxygen addition recipe failed in sustaining the (100) orientation for a long time growth of over 100h. In figure 6, (111) oriented crystals dominate the surface feature of the finished sample. The initial (100) oriented crystal squares totally disappeared.



Figure 6. Long time growth of oxygen addition recipe. Left: 10X, Right: 50X.

1.2.2 Oxygen addition recipe after BEN (continued)

In the above experiments of oxygen related recipe, we only focused on low methane concentration of 2%. Even though the growth rate was low, the surface morphology after the growth with oxygen recipe was very promising, where all (100) grains were merging together without boundary. To extend the growth region even further, we focused on high methane concentration of 8% during this month. Without adding oxygen, the achieved diamond was of poor quality with high level of graphitic impurity. Fine tuning of oxygen addition and temperature will be performed. However, the effects of these two parameters are related. We will first explore the influence of oxygen addition from low to high. As for the temperature, two points of 950°C and 1050°C will be picked to compare the effects.

1.2.3 Experiments

We tried the recipe of $\text{CH}_4/\text{O}_2/\text{H}_2 = 20/1/230$ sccm at 1050°C with HOD substrate. Shown in figure 7 (left), considerable twin features appear together with the HOD background. After adding more oxygen to 2 sccm, while keeping other parameters unchanged, much cleaner surface was achieved, as shown in figure 7 (right). Adding oxygen can suppress the twin formation through effective etching of graphitic impurities. However, the growth time in this round was set as short as 1.5h. In the next run, we will increase the oxygen addition more, and extend the growth time further.

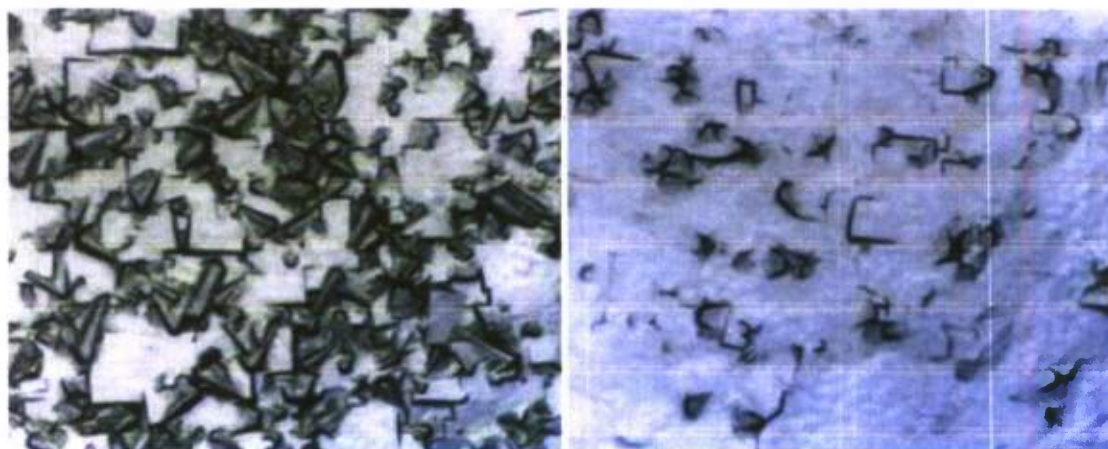


Figure 7. Growth result of $\text{CH}_4/\text{O}_2/\text{H}_2 = 20/1/230$ sccm (left), and $\text{CH}_4/\text{O}_2/\text{H}_2 = 20/2/230$ sccm (right)

While keeping most parameters unchanged, we increased oxygen addition to 3 sccm and extended the growth time to 14 h. The result is shown in figure 8, where all initial HOD feature disappeared. Three factors should be considered to explain the result. First, the initial HOD surface morphology was of lower quality, which was manifested by broad grain size distribution and non-uniform grain orientation distribution. Secondly, the growth temperature of 1050°C may be a little too high, which gives a low ALFA value. And such low ALFA value usually will accompany a higher chance of twin formation. Thirdly, oxygen addition may still be not enough to etch all boundary graphitic impurities, and it finally will lead to serious twin formation after long time growth.

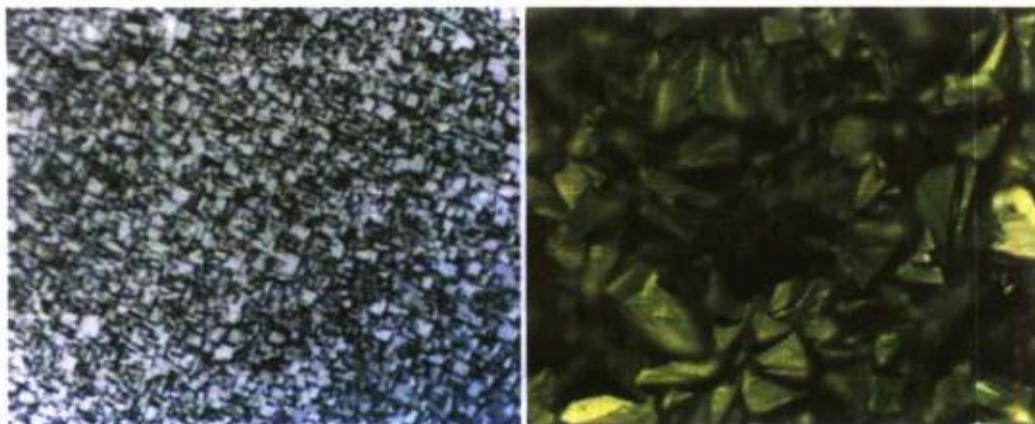


Figure 8. Growth result of $\text{CH}_4/\text{O}_2/\text{H}_2 = 20/3/230$ sccm on HOD, with initial HOD substrate (Left) and after growth (right).

Based on above analysis, we reduced growth temperature from 1050°C to 950°C in this run. The growth time was still set as 14h. The diamond growth before (figure 9(left)) and after (figure 9(right)) were illustrated. Compared with previous runs, the growth result of current run had much improvement. Together with sporadic twin formations, cleaner HOD feature was kept after 14h growth. The good quality of the achieved HOD sample can be judged from its narrow diamond peak and flat background in the Raman spectrum, shown in figure 10. As a comparison, the Raman spectrum of the twins shows a higher background level and broad diamond peak, which is consistent with the typical low quality of twins. The result of this run is a proof that lower deposition temperature helps in suppressing twin formation. To completely eliminate surface twin formation, we will add more oxygen in the next run.

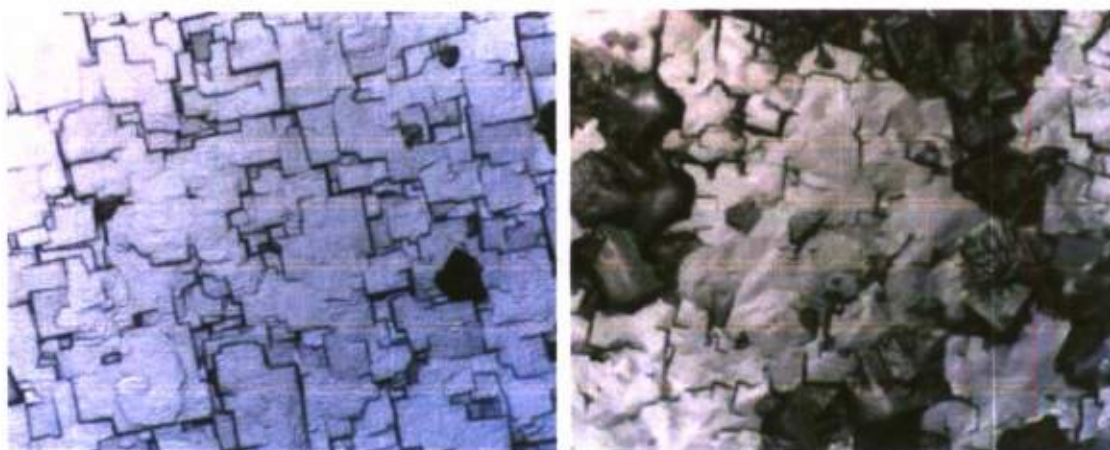


Figure 9. Growth result of $\text{CH}_4/\text{O}_2/\text{H}_2 = 20/3/230$ sccm on HOD with temperature 950°C . Before (left) and After (right).

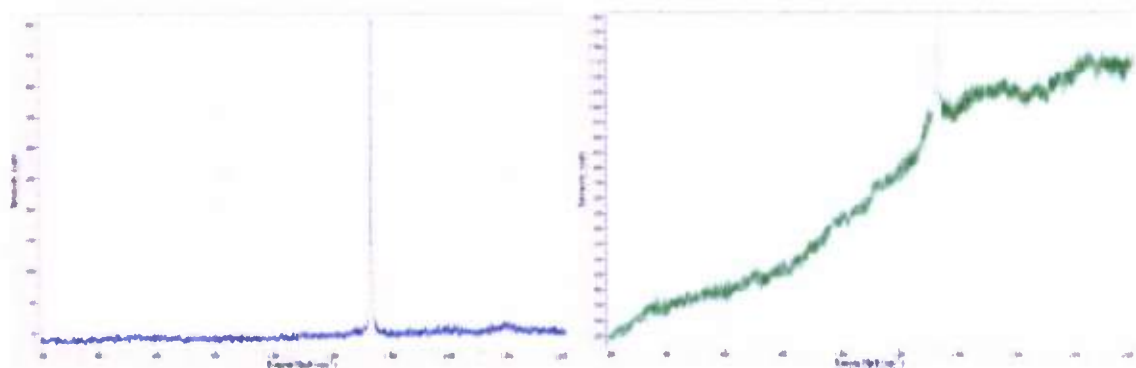


Figure 10. Raman spectrum of HOD (left) and twin (right).

While keeping main setting parameters unchanged, the oxygen will be added from 3sccm further to 4sccm. The chamber pressure will be set at around 170mbar. In such relatively high chamber pressure, the small size of plasma will not be able to uniformly heat the entire 2'' silicon wafer. This will lead to a 100°C temperature gradient from wafer center to edge. In other words, if the wafer center temperature is 1050°C, the temperature at half radius position will be around 1000°C, and the temperature close to wafer edge will be 950°C. Even though, the surface morphology transition from center to edge can also be utilized to evaluate the temperature influence in this range, as shown in figure 11. It is obvious that the density of twin formation drops from center to edge with clean HOD formation in the wafer edge area. This also indicates an optimal growth temperature of 950°C.

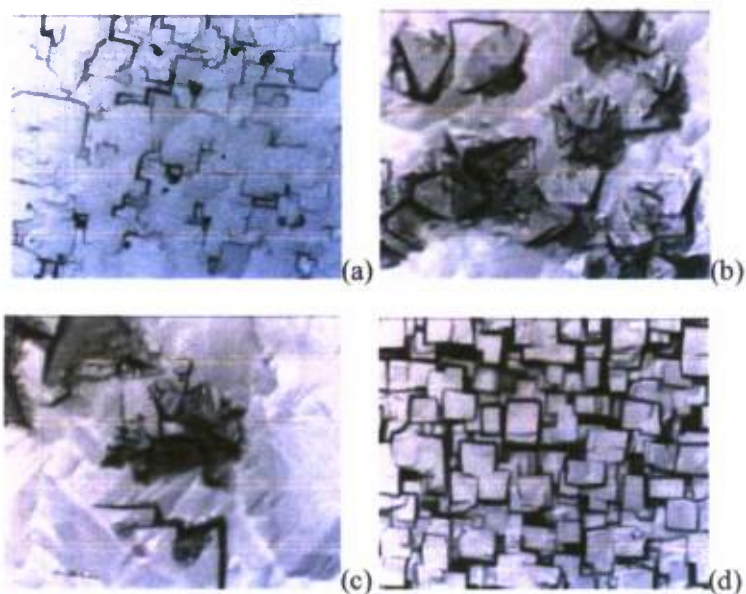
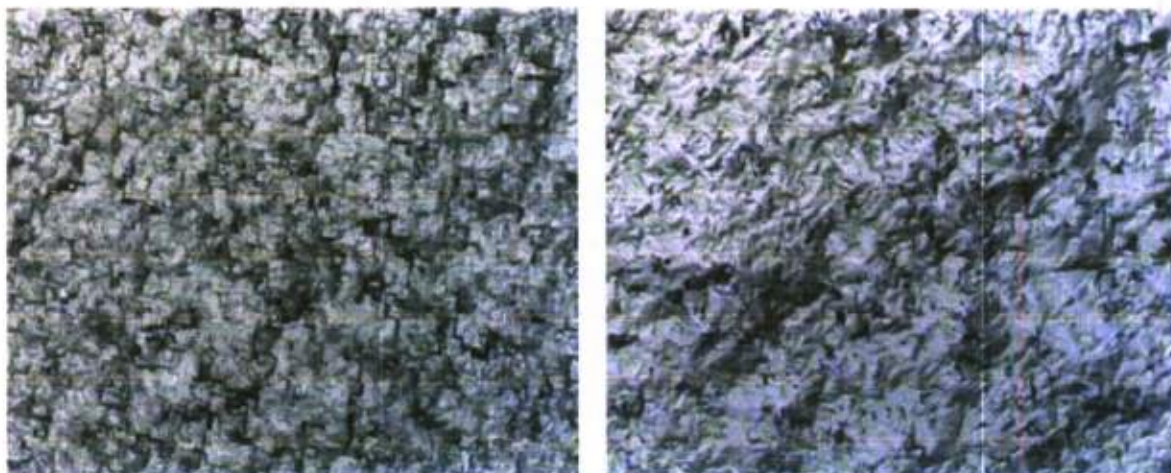


Figure 11. $\text{CH}_4/\text{O}_2/\text{H}_2 = 20/4/230$ on HOD, 1050°C-950°C, 175mbar. (a) Initial HOD substrate. (b) Wafer Center at 1050°C. (c) Wafer middle at 1000°C. (d) Wafer edge at 950°C.

Based on above experiments, we then set the growth condition on HOD substrate as $\text{CH}_4/\text{O}_2/\text{H}_2 = 20/4/230$ sccm, 950°C, 175mbar, on Moly holder, 14h. The HOD growth result was very promising with no twin formation and effective grain merging, as illustrated in figure 12.

(10X)



(50X)

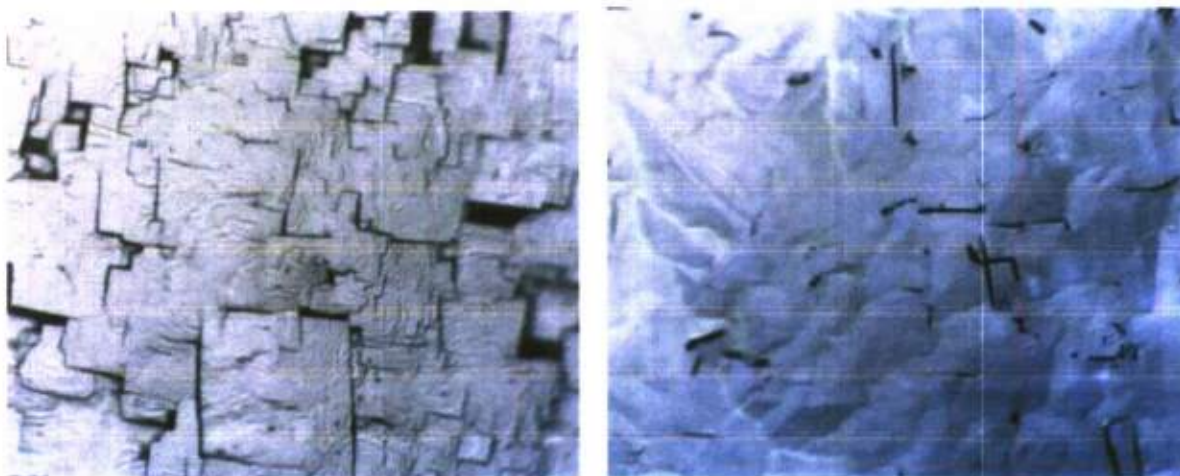


Figure 12. Growth on HOD substrate with $\text{CH}_4/\text{O}_2/\text{H}_2 = 20/4/230$ sccm, 950°C , 175mbar, on Moly holder, 14h. Two magnification ratios of 10X and 50X were shown, with comparison of Before (Left) and After (Right) growth.

Shown in figure 13(a), the flat background and sharp peak of the Raman spectrum suggests a high quality of the after-growth HOD sample. However, the magnified diamond peak in figure 13(b) demonstrates a doublet structure. As we know, diamond crystal will give a typical Raman peak at 1332 ($1/\text{cm}$). If the diamond grain is under tensile stress, the peak will have a red-shift. Or if the diamond grain is under compressive stress, the peak will have a blue-shift. With the current oxygen recipe, the level of grain boundary impurity has been well controlled. As a result, diamond grains merge together with strong bonding force, which conversely generates significant stress on the diamond grain itself. Under the smooth surface, there are numerous unseen merging grain boundaries. The splitting of the diamond Raman peak reflects the large stress difference of the merging grains.

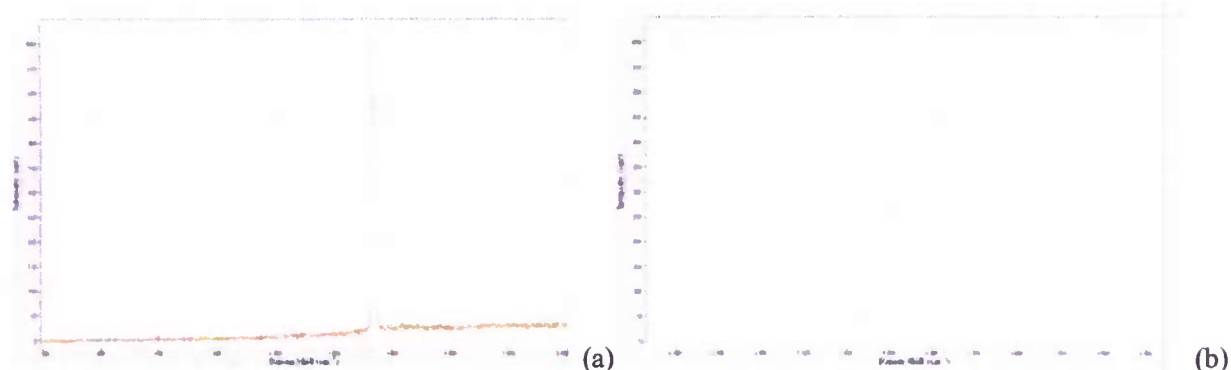


Figure 13. Raman spectrum of the after-growth HOD sample. (a) 200-2000 (cm^{-1}). (b) Magnified peak.

As a summary, we have explored oxygen related recipe for HOD growth under high methane concentration of 8%. It has been confirmed that oxygen addition can effectively etch the graphitic impurities even under such high methane concentration. Also, lower growth temperature led to lower density of twin formation. After a series of experiments, we have realized satisfactory growth on HOD substrate under optimal conditions of $\text{CH}_4/\text{O}_2/\text{H}_2 = 20/4/230$ sccm, 950°C , 175mbar. The average growth rate was $5\mu\text{m/h}$.

1.3 Developing an oxygen-containing recipe on single crystal diamond substrate.

We have developed an oxygen-containing recipe for HOD growth aiming at reducing the graphitic impurity level and maintaining the (100) diamond crystal orientation by suppressing the twinning formation during the long-term deposition of diamond. The recipe consists of 8% CH_4 , 0.1% N_2 , 0.5% O_2 , and 91.4% H_2 . The nitrogen concentration is planned to be lowered further so that the nitrogen incorporation in the diamond can be minimized. This recipe has been implemented on a HTHP single-crystal diamond substrate to test if the diamond single crystal structure can be maintained.

Shown in Figure 14, the homoepitaxial diamond layer on a $4\text{X}4\text{ mm}^2$ HTHP diamond substrate exhibits a clean and twin-free top surface. Due to the oxygen addition, although the methane concentration is higher than it used to be, the diamond growth rate is moderate ($\sim 15\mu\text{m/hour}$) compared with non-oxygen recipe which can reach more than $30\mu\text{m/hour}$ growth on single-crystal diamond.

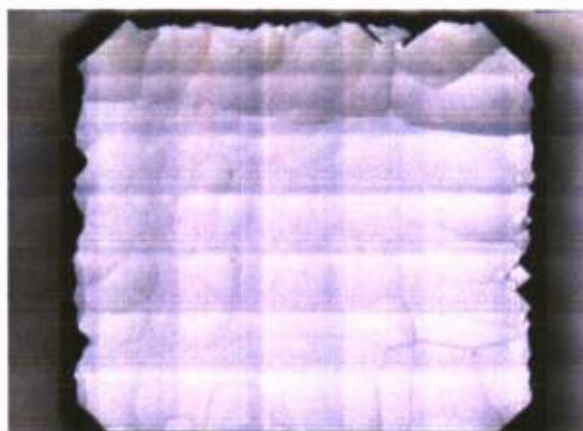


Figure 14. Microscopic images of the surface of the homoepitaxial diamond layer.

A closer look at the epitaxial diamond layer can be found in Figure 15. The SEM photographs show microscopic smooth diamond surface without any twining and renucleation. The diamond deposition alpha parameter can be estimated to be between 2 and 2.5 from the truncating plane angle in the sample corner shown in Figure 15(b).

The Raman spectroscopic study result of the epitaxial diamond is presented in Figure 16. Comparing with the 100 ppm N_2 HOD sample reported in the previous report, the quality of the epitaxial diamond layer is significantly improved, which is indicated by the much smaller full width half maximum (FWHM) values (2.6 cm^{-1} vs. 4.7 cm^{-1}) of the diamond peaks at 1332 cm^{-1} (Figure 16(b)). This result is partially due to the single crystal nature of the epitaxial layer. It can also be observed that the nitrogen incorporation levels in the diamond is still high, which is represented by the strong Raman peak around 1450 cm^{-1} . Given a much lower nitrogen concentration (100 ppm) used for HOD growth, there is still a room for further reduction of the nitrogen in the reactive gas mixture and the optical transmittance of the diamond layer can be improved further.

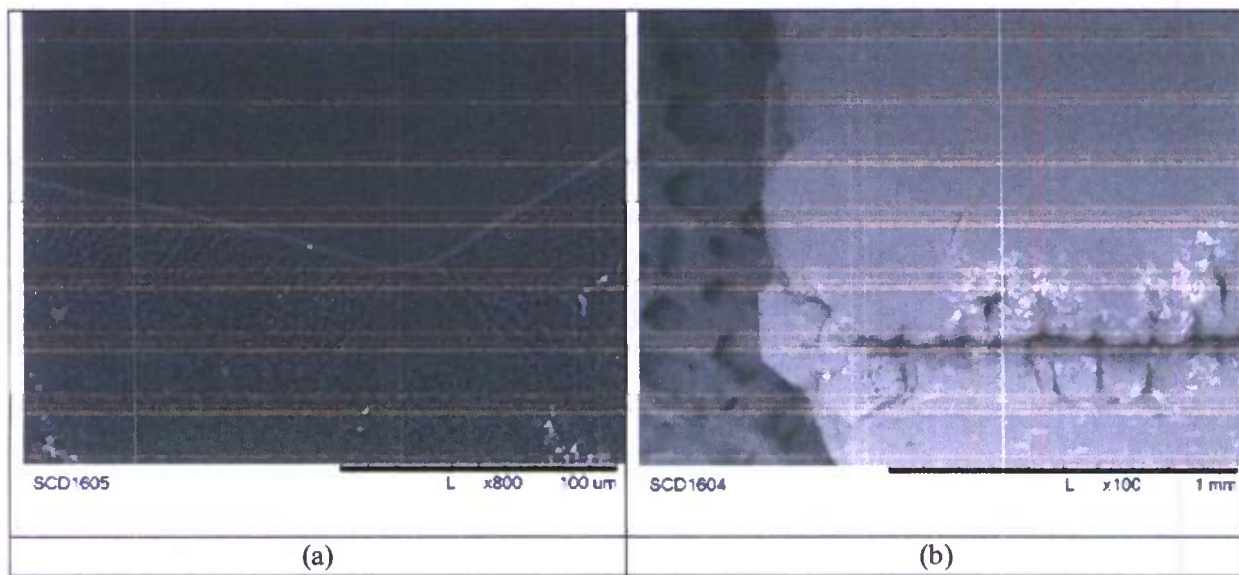
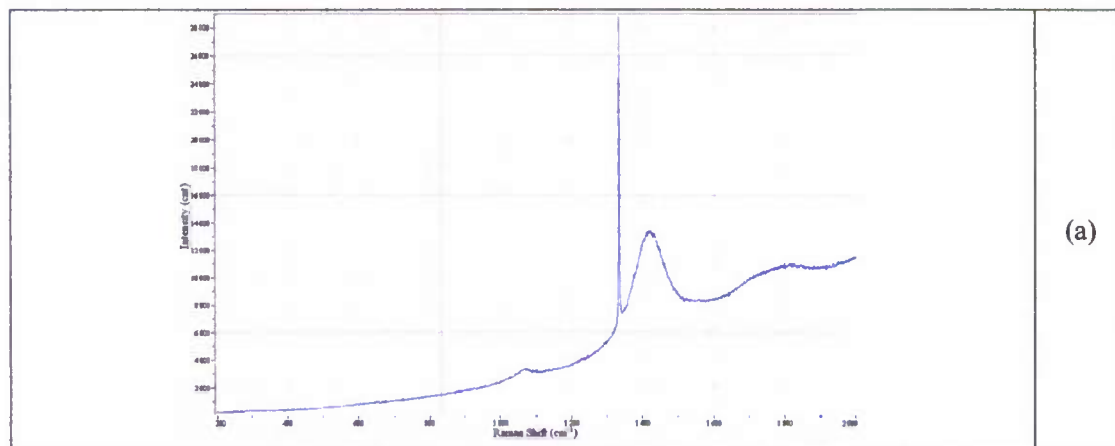


Figure 15. SEM photographs of the homoepitaxial diamond layer. (a) 45° tilting view of the diamond surface. (b) 45° tilting view of the sample corner.



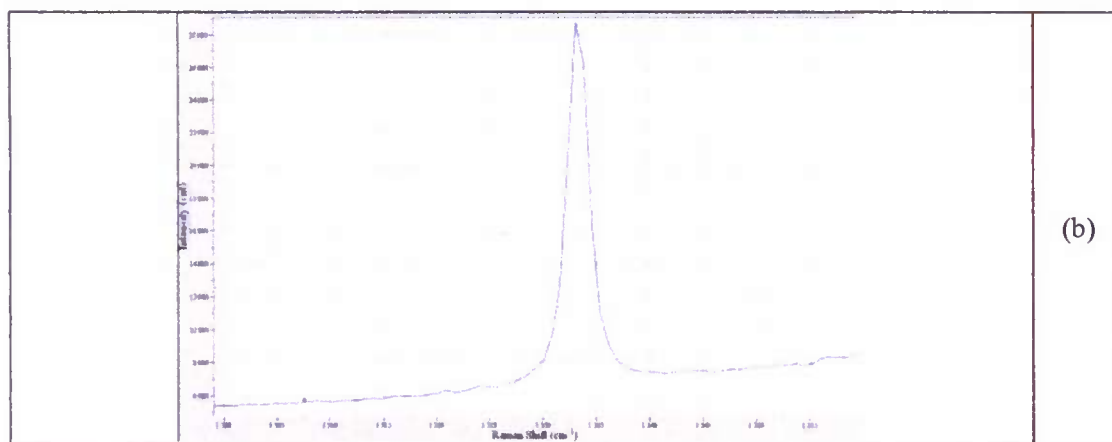


Figure 16. Raman spectrum of the epitaxial diamond. (a) full view, (b) zoom-in view of the diamond peak.

1.4. Epitaxial Chemical Vapor Deposition of Single Crystal Diamond

Above, we reported successful deposition of epitaxial single crystal diamond (SCD) on top of high-temperature-high-pressure (HTHP) synthesized SCD chips using 6% CH_4 /94% H_2 /2800ppm N_2 gas mixture at 1180 °C with chamber pressure of 170-200 mbar with a high diamond growth rate of 36 $\mu\text{m}/\text{hour}$. The twin formation during the course of CVD process was completely suppressed, leading to a clean and smooth as-grown diamond top surface. Raman spectroscopic study showed good diamond quality and phase purity of the epitaxial layer. However, the nitrogen incorporation was high and the epitaxial layer exhibited dark brown color due to the strong photon absorption by the substitutional nitrogen in the yellow wavelength range.

As a crucial factor of this project, we proposed the growth of epitaxial SCD on top of AFB[®]-bonded SCD seeds in order to expand the size of the final SCD product. We have carried out preliminary experiments with a goal of testing the merging of epitaxial SCD layers originating from two adjacent HPHT diamond seeds. During the CVD epitaxial deposition process, the two HTHP diamond chips were simply put side by side on the sample holder without any physical or chemical bond in between. Two different diamond growth recipes were used. SEM and optical microscopic studies were carried out to examine the morphology and microscopic structure of the epitaxial SCD layers as well as the merging between them. Raman spectroscopic study was also performed to examine the quality and impurity level of the epitaxial SCD.

1.4.1 Epitaxial SCD deposition using high nitrogen concentration recipe

One experiment was carried out using the previously reported recipe of 6% CH_4 /94% H_2 /2800ppm N_2 gas mixture at 1180 °C with chamber pressure of 170-200 mbar. The total deposition time was 16 hours resulting in an epitaxial SCD layer of $\sim 600 \mu\text{m}$, and the initial gap between the two HPHT SCD seeds is estimated to be 50 μm wide. The CVD epitaxial results are shown in Figure 1.1. From the optical microscopic image in Figure 1.1(a) it can be observed that the merging of the two epitaxial layers is poor. The gap is still obvious and the boundary line is in a zigzag shape. However, under the SEM with a higher resolution, the boundary line appears to be partially vanished indicating that the two epitaxial SCD layers have partially coalesced together (Figure 17(b&c)). The cross section of the

epitaxial layer, which is shown in Figure 17(d), was also examined using SEM after physically breaking the two seeds apart. A clear single crystal cleavage feature with layered structure is observed.

We think the main reason of this poor coalescence is the rough side wall of the epitaxial SCD layer. It can be observed from Figure 17(c) the side walls of the trench consist of many small diamond grains formed by re-nucleation mechanism, keeping the trench from healing by itself.

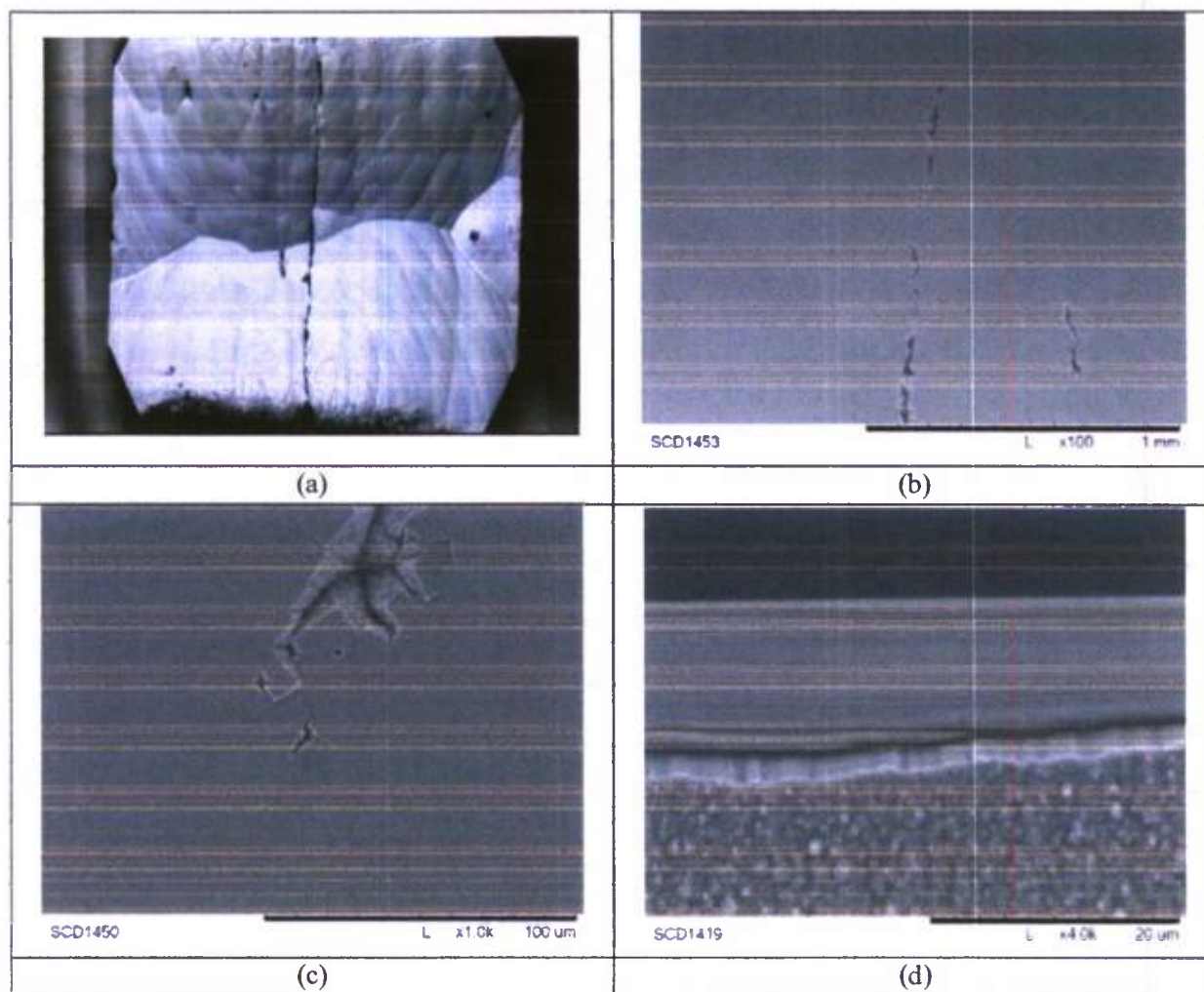


Figure 17. Digital and SEM photographs of the epitaxial diamond layer. (a) optical microscopic image of a overall view, (b, c) SEM photographs of part of the merging line, and (d) SEM cross section view of the merging line after physically breaking the two seeds.

1.4.2 Epitaxial SCD deposition using low nitrogen concentration recipe

A second experiment was carried out using a recipe which was developed previously for highly oriented diamond (HOD) growth, of 3% CH₄/97% H₂/200ppm N₂ gas mixture at 1050 °C with chamber pressure of 120 mbar. It has been proven by the HOD deposition experiments that this recipe is suitable for promoting the coalescence among neighbor diamond grains in a microscopic level. Moreover, the twinning formation during the CVD process can be successfully suppressed by using this recipe. One drawback of this recipe is that it requires very precise temperature control during the diamond deposition

because the temperature window for (100) diamond growth under this condition is relatively narrow ($\sim 20^\circ\text{C}$). The experimental results are shown in Figure 18. The total deposition time was 8 hours resulting in an epitaxial SCD layer of $\sim 80\ \mu\text{m}$ and the initial gap between the two HPHT SCD seeds is estimated to be $50\ \mu\text{m}$ wide as well.

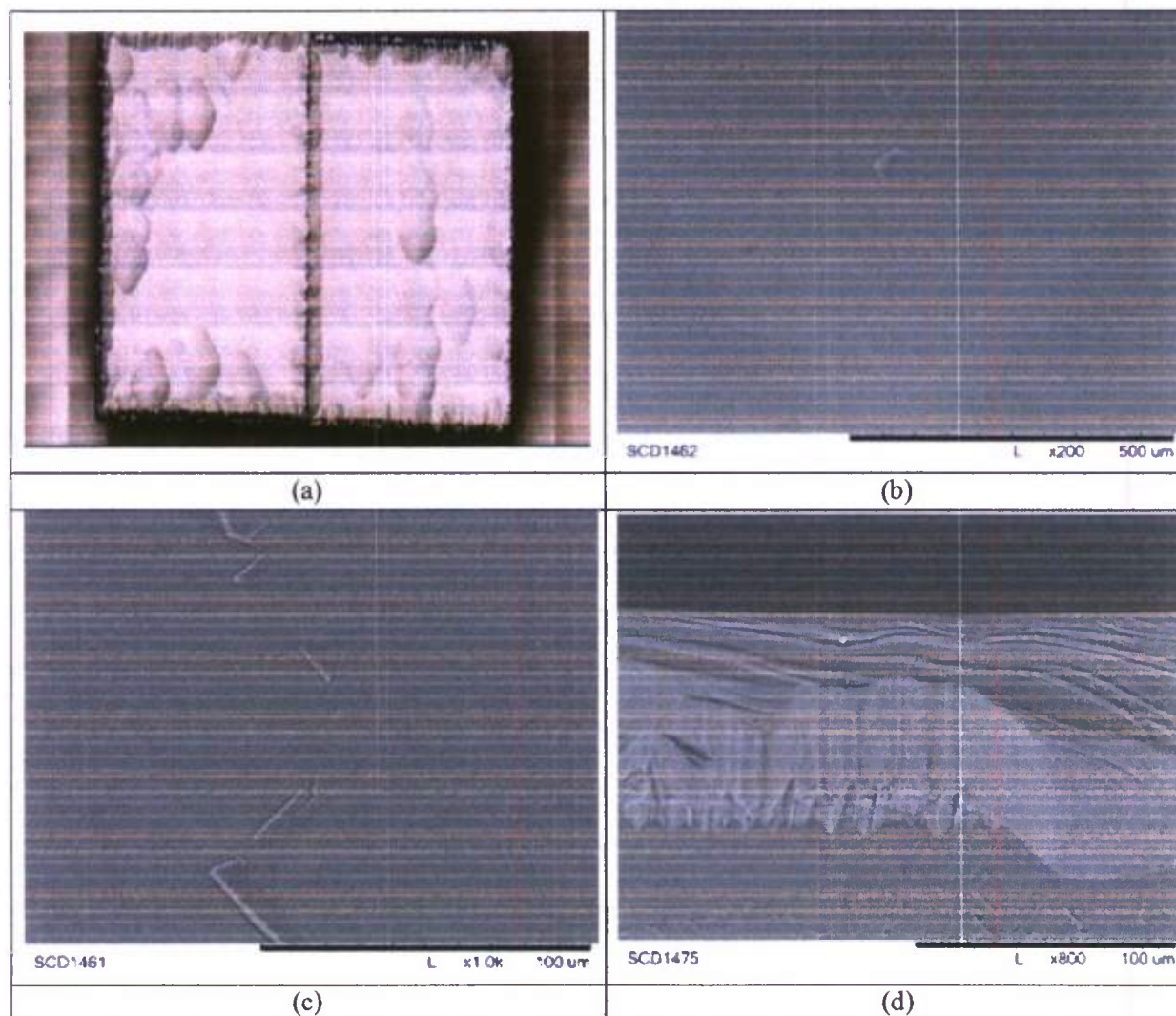


Figure 18. Digital and SEM photographs of the epitaxial diamond layer. (a) optical microscopic image of an overall view, (b, c) SEM photographs of part of the merging line, and (d) SEM cross section view of the merging line after physically breaking the two seeds.

It can be observed from Figure 18 that the coalescence between the two epitaxial diamond layers from the two adjacent HPHT SCD seeds has been promoted. The boundary line is vanishing with a few polycrystalline diamond grains embedded along the line. The cross section view of the epitaxial layer, along the boundary line after being physically broken, exhibits single crystal structure indicating the successfully merging of the epitaxial layers. We believe that these polycrystalline grains generated at the beginning of the epitaxial growing process will be overwhelmed and embedded completely inside the bulk epitaxial SCD layer after long term growth, leading to a smooth, fully coalesced boundary line. These two epitaxial layers will merge together forming a one-piece single crystal layer. This growth

condition can be further optimized by lowering the substrate temperature to minimize the formation of the polycrystalline diamond grains along the edge of the HPHT seeds. Therefore, the two epitaxial SCD layer will be ready to merge together without the obstruction of the polycrystalline diamond grains.

The Raman spectrum collected from the epitaxial SCD layer is shown in Figure 19. It is clear that the diamond peak is very sharp with a small full-width-half-maximum (FWHM) value of $\sim 2.5 \text{ cm}^{-1}$, indicating very good diamond quality and low defect density. Moreover, the broad peak around 1450 cm^{-1} is much weaker than that of the high nitrogen concentration sample, meaning a much lower nitrogen incorporation level in this epitaxial SCD layer.

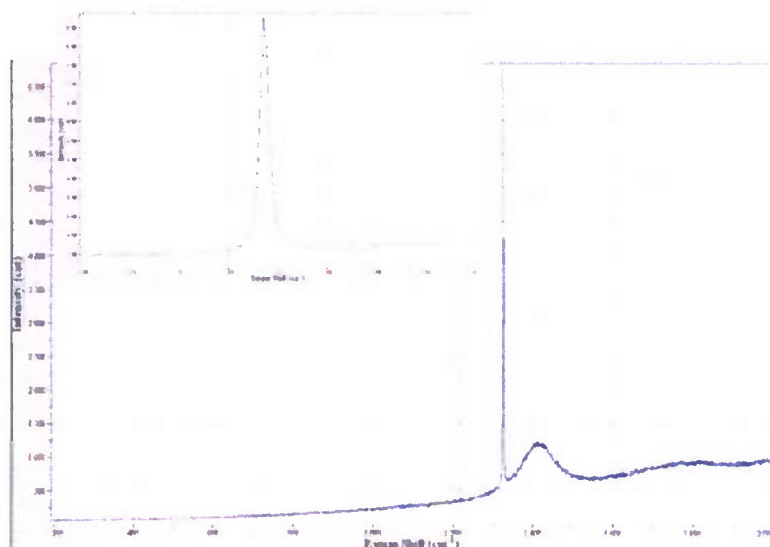


Figure 19. Raman spectrum collected from the epitaxial SCD layer with a zoom-in view of the diamond peak at 1332 cm^{-1} .

It has been demonstrated that the epitaxial SCD layer growing on top of two individual SCD seeds can merge together to form a single crystal diamond layer, even though there are microscopic gap and height difference in between the two growing surface. If the two SCD seeds are AFB[®]-bonded with much smaller gap width, height difference, and orientation mismatch, the merging effect should be greatly improved.

2. Optical coating of high laser damage threshold

2.1 Coating for YAG crystals

Sample preparation consisted of working in class 100 laminar flow bench to perform all pre-processing steps before the sample to be coated is loaded into the coating system. The preparation was started with pre-inspection and pre-cleaning followed by mounting the sample in an adjustable sample holder. After mounting, the samples were final cleaned and a final pre-process inspection was completed. The samples were then transferred from the laminar flow bench to the class 100 coater cleanroom. In the coater cleanroom, the samples were then removed from the transfer container and loaded into the BAP800

coating system. The results of the sample preparation were good, as shown in the figure 20. The coating results were a smooth coating that was clean, defect-free and with good adhesion.

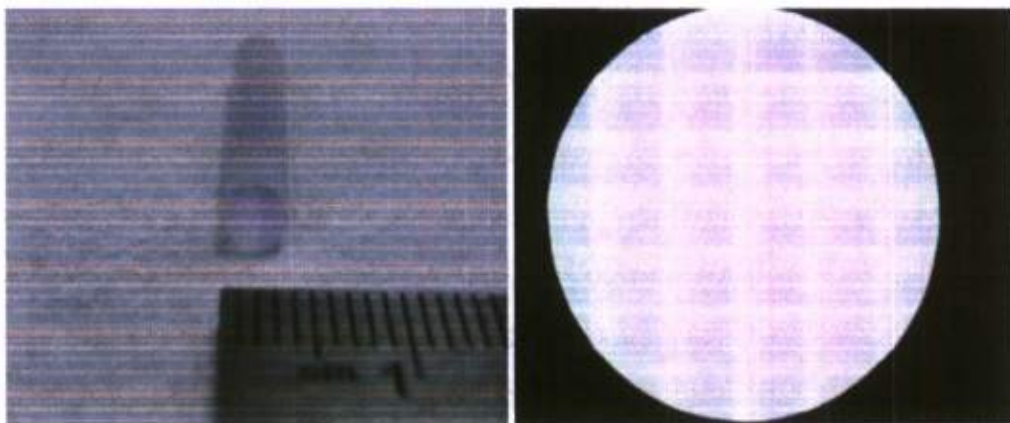


Figure 20. (a) Clean and defect-free 4mm Dia. X 20mm L. YAG end-face. (b) Microscope image of clean and defect-free 4mm Dia. X 20mm L. YAG end-face

2.1.2 Coating Process

A good coating process was demonstrated in the historical data trending of the BAP800 coating system. In the historical data trending curves, a comprehensive image of a coating process is given in graphical representation as in figure 21. A description of the pens, the parameters which they represent, and their characteristics of good operation are listed below:

Pen #1 "CRYSTAL_RATE_SCL" - The deposition rate measured by the six position quartz crystal monitor. The curve of Pen#1 it is not visible in this resolution; however, it was checked after each coating layer and was found to indicate acceptable rate control.

Pen #2 "CRYSTAL_MON_THICK_1" - The layer thickness as measured by the six position quartz crystal monitor. The linear increase in thickness indicated a stable and correct deposition rate. The instantaneous changes between deposition layers indicated that the six position changer was being switched to another crystal with each layer.

Pen #3 and Pen #4- "MFC_1_FLOW" and "MFC_2_FLOW" - The mass flow controllers are shown as they admit process gas to the deposition chamber. Pen #3 had a steady line, indicating that the ion source gas inlet was receiving a constant flow at the proper set flow rate. Pen #4 had a varying line indicating that the mass flow controller was modulating to maintain a steady process pressure in the chamber. Usually, it is most desirable to have both these curves vary as little as possible after they have reached a control set point. In the case of Pen #4- MFC_2_FLOW, the first and third curves were very steady when source 1 was in use. The second and fourth curves showed modulation when source 2 was in use. The modulation seen here is normal, because in electron beam evaporation of Silicon, the material is difficult to evaporate due to the tunneling effect of the electron beam. The effects are reflected in the process pressure control.

Pen #5 and Pen #6- "DEP_1_FIL_AMP" and "DEP_2_FIL_AMP" - The electron beam filament current was shown for each individual source when it was in use. These curves modulated very little when the

desired deposition rate was reached. Though the curves will modulate very little, they tend to vary significantly in current, because filament life and amount of source material being used or depleted significantly affects this parameter.

Pen #7 and Pen #8- "SHUT_1_CLOSE" and "SHUT_2_CLOSE"- The shutter closed inputs are used to determine the shutter open time. From this, the deposition time and rate can be determined. The deposition time and rate are critical process parameters that strongly affect film characteristics and thickness control.

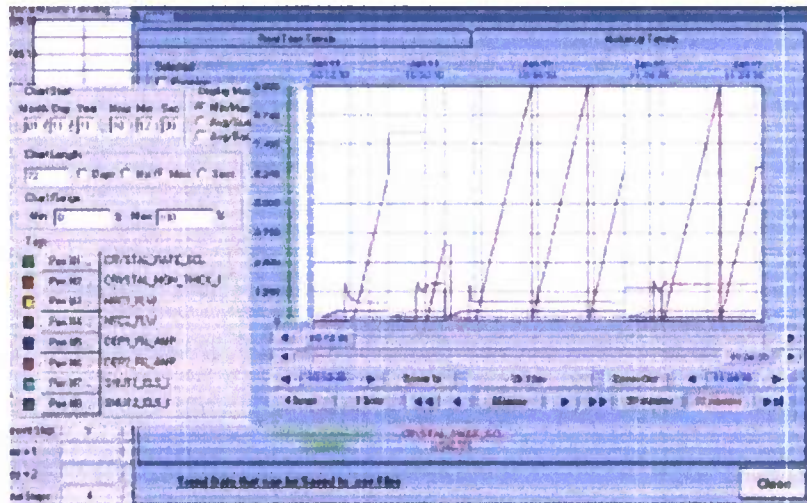


Figure 21. BAP800 Historical data trending of coating process.

2.1.3 Coating measurement result

Sample coating thickness was measured using 1" silicon wafers as thickness witness samples because the 4mm diameter end faces were too small an area to obtain a measurement from. The results were well within the process design specifications as shown in figure 22.

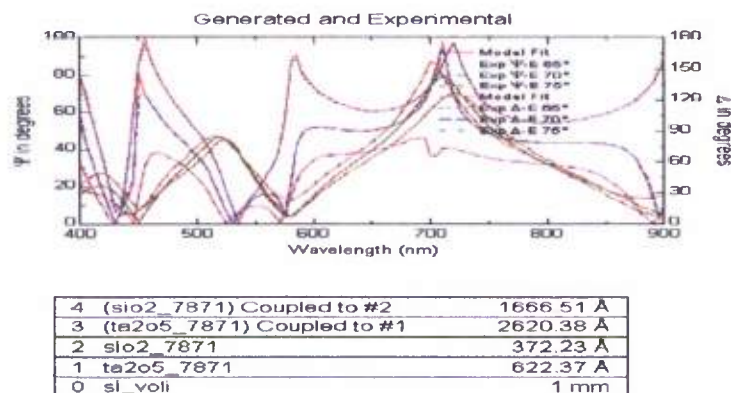


Figure 22. Ellipsometer curve of 1" silicon wafer witness sample.

Spectrophotometer data shown in figure 23 was provided by measuring the YAG witness sample. Compared with the design target of AR@808nm (<1%) and AR@1064nm (<0.1%), the coating has successfully reached design target at 808nm. However, its AR performance at 1064nm fell short for around 0.5%, which came mainly from coating absorption. Therefore, we plan to increase the working chamber pressure in the next try. Because the working gas is oxygen, the higher chamber pressure will mean more sufficient oxidization of the coating material, which in turn will reduce the optical absorption further.

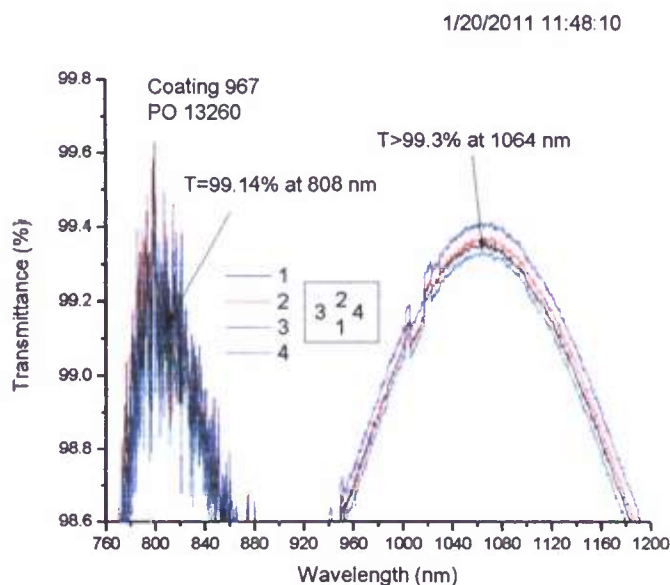


Figure 23. Spectrophotometer curve of witness sample.

2.2 Coating for Vanadate crystals

2.2.1 Introduction

The coating target is AR@808nm($R < 1\%$) and 1064nm($R < 0.1\%$). However, the birefringent nature of vanadate crystal needs to be considered in the coating design.

For YVO₄, its optical properties can be summarized as the following.

Refractive index of YVO4,

Positive ($n_e > n_o$) uniaxial crystal

$$n_o^2 = 3.77834 + 0.069736/(\lambda^2 - 0.04724) - 0.0108133\lambda^2$$

$$n_e^2 = 4.59905 + 0.110534/(\lambda^2 - 0.04813) - 0.0122676\lambda^2$$

Refractive index of e-beam:

$$n_e^2(\theta) = \frac{n_o^2 n_e^2}{n_o^2 \sin^2 \theta + n_e^2 \cos^2 \theta}$$

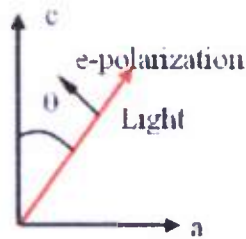
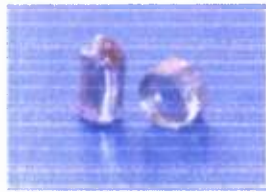


Figure24. Illustration of YVO4 crystal (left) and birefringent index nature

Shown in figure 25, we have proposed three designs here based on either e-ray index curve or o-ray index curve. Left (design I): AR coating designed for o-ray index curve, but tested under e-ray input. Right (design II): AR coating designed for e-ray index curve, but tested under o-ray input. Generally, the AR performance will decay for around 0.2% with different ray input. And the design based on e-ray index curve gives better tolerance as shown in the right figure.

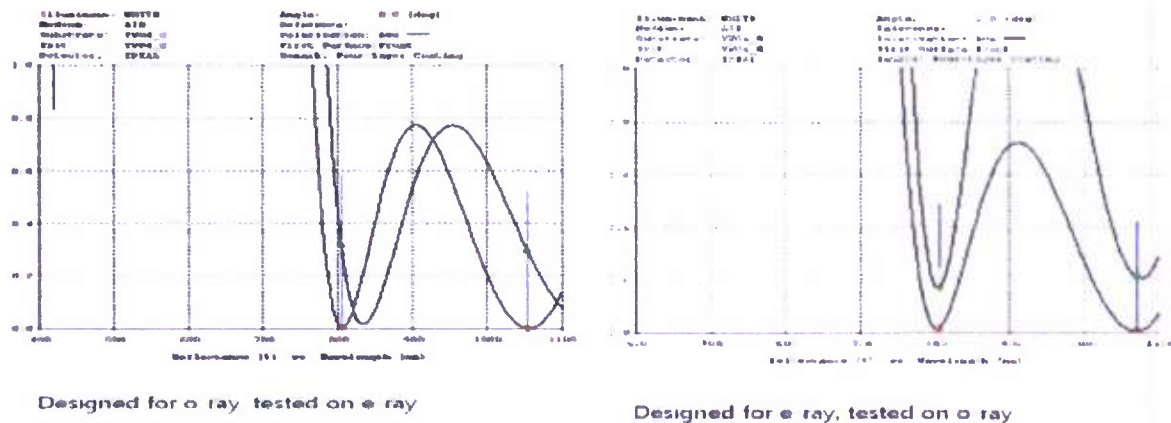


Figure 25. Design I (left) and design II (right) of AR coating on vanadate crystal

At the same time, we have another choice of using the average index values of e-ray and o-ray. The design-III together with its deviation to e-ray and o-ray is shown in the next figure. As we can see in figure 26, the error was around 0.1% for both e-ray and o-ray.

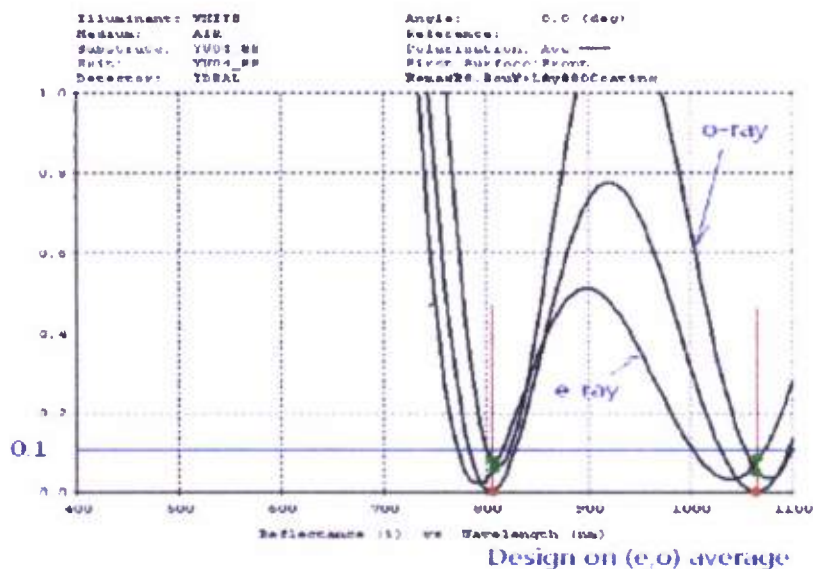


Figure 26. Design III of AR coating on vanadate crystal

As a summary, the following table shows the error of the above three designs.

	<i>e-ray</i>	<i>o-ray</i>
<i>Design I</i>	0.3%	0
<i>Design II</i>	0	0.2%
<i>Design III</i>	0.1%	0.1%

The final decision was to use the e-beam index curve for coating design. Here, the performance at 1064 nm is more important than 808 nm. The laser of a-cut Nd: YVO₄ prefers e-polarization (parallel to c-axis). Input light of 808 nm is a pump and has less effect on the laser performance.

2.2.2 AR coating design for Vanadate crystal

Thorough searching of the possible AR coating design has been performed with a program written on labview platform. The program has been proven very effective in identifying all promising coating designs. The obtained prototypes will then be optimized on coating design software TFCAL. The calculation took one week to finish. As shown in the following, we got one design for single layer coating, one design for two layer coating, four designs for three layer coating, and six designs for four layer coating. The pro and con for these designs have been briefly discussed in the following. The criteria in judging a coating design should first be simple structure and thin total thickness. More considerations will be discussed in the later sections.

2.2.2.1 Single layer design.

Illustrated in figure 27, this design utilizes the interference pattern of 7 QW thickness SiO₂ coating. Even though it can reach the design target at R@1064nm, the reflectivity at 808nm will be around 2%. The

spectrum has relatively low error tolerance, which was related with the narrow width of the “valley”s at 808nm and 1064nm. Although the coating is too thick ($>1\mu\text{m}$), the fact that it uses only one coating material is still interesting, especially this coating material is low absorption low index SiO_2 .

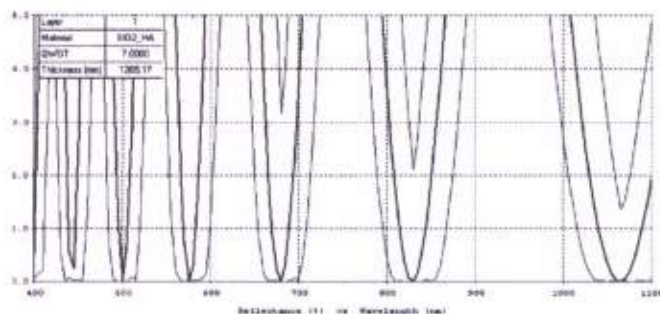


Figure 27. Single SiO_2 layer AR design for vanadate crystal

2.2.2.2 Two layer design

Illustrated in figure 28, besides reaching the design target at both 808nm and 1064nm, the simple structure is the advantage of this design. However, too thick Ta_2O_5 layer may give strong light absorption. It is also undesirable to have high reflectivity between 808nm and 1064nm, which reaches over 40%.

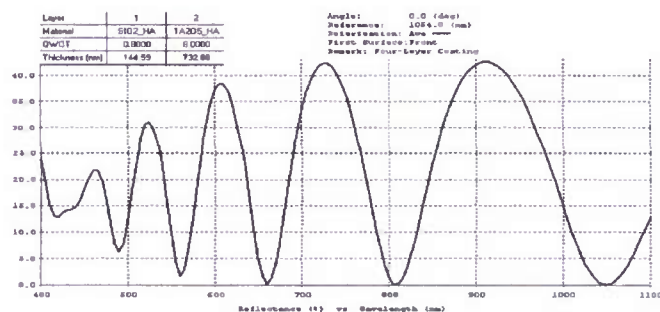


Figure 28. Two layer AR design for vanadate crystal

2.2.2.3 Three layer design

Shown in figure 29, this design is very attractive in having reasonable total thickness and very good anti-reflection performance in a wide range between 800nm and 1100nm ($<1\%$). However, the first layer of SiO_2 is as thin as 20nm. Even though it can still be manufactured reliably, the potential risk lies in the adhesion between this thin layer and the substrate surface. Such thin layer may not sustain the relatively strong compressive stress of the coating. This coating structure was adopted for the first batch of samples.

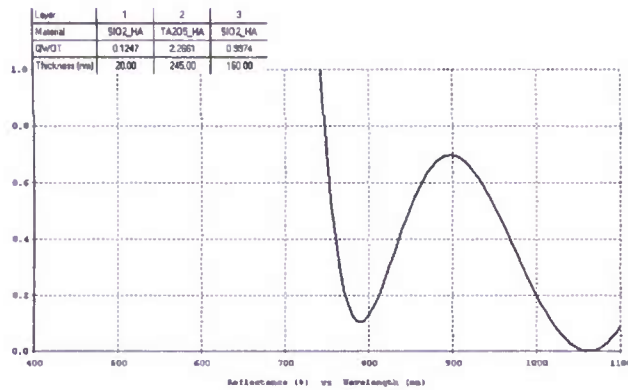


Figure 29. Three layer AR design for vanadate crystal

One simple solution is to add certain thickness buffer layer of Ta₂O₅ under thin SiO₂ layer. As the refractive index of Ta₂O₅ is very close to that of YVO₄ crystal, its influence to the following AR coating design should be very limited, which is confirmed by the similar thickness structure of the out three layers. Shown in figure 30, this coating structure will be tried on the second batch of coating sample.

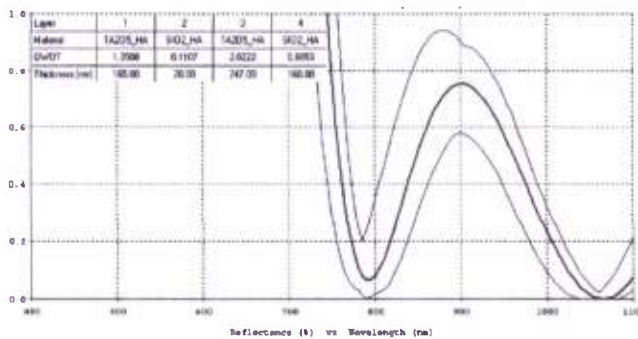
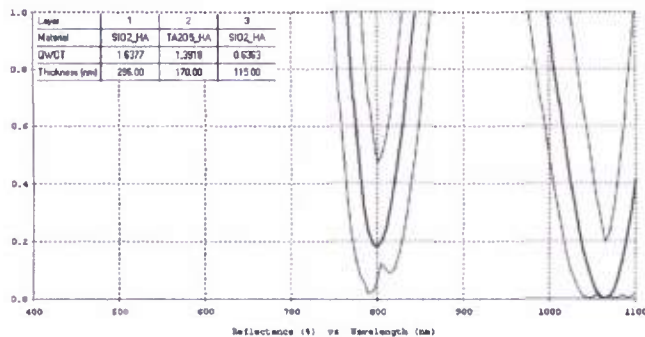


Figure 30. Optimized three layer AR design for vanadate crystal

Shown in figure 31, the following two designs of three-layer structure are of reasonable total thickness and can reach the anti-reflectivity design target, even though not as good as the above one.



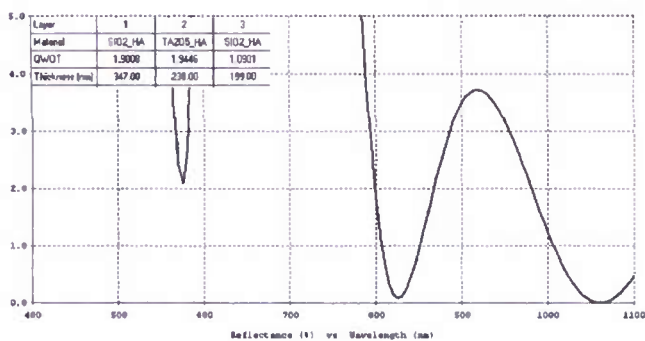


Figure 31. Three layer AR designs for vanadate crystal. (a) above. (b)below.

As in figure 32, the three-layer AR design has the advantage of very thin Ta₂O₅ layer. Considering the stronger light absorption of Ta₂O₅ relative to SiO₂, this design may be a possible choice.

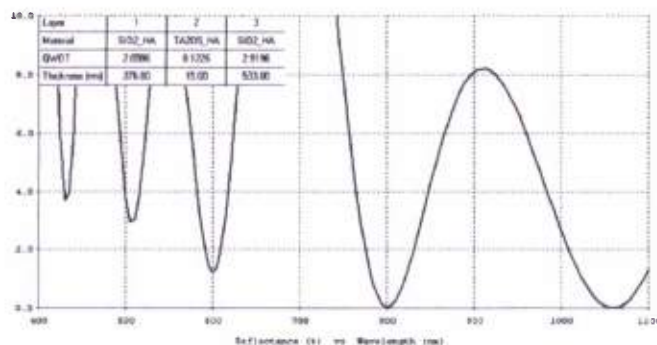


Figure 32. Three layer AR design for vanadate crystal with very thin Ta₂O₅ layer (15nm).

2.2.2.4 Four layer design

Besides the four-layer AR design mentioned above, another six designs of four-layer structure were introduced in the following, which were listed sequentially according to their coating performance. Illustrated in figure 33,34,35, the total thickness of these coatings were all reasonable, between 500um and 1000um. All can be manufactured without much difficulty.

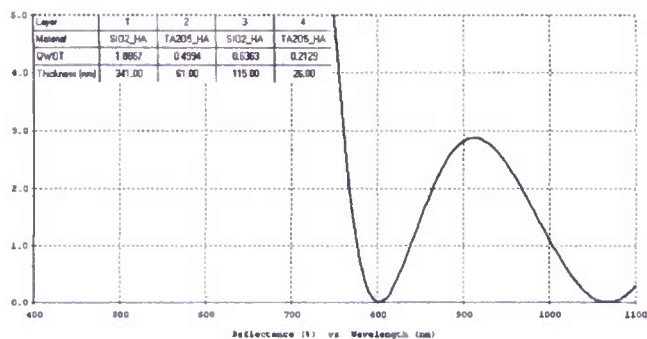


Figure 33. Four layer AR design for vanadate crystal. (a)

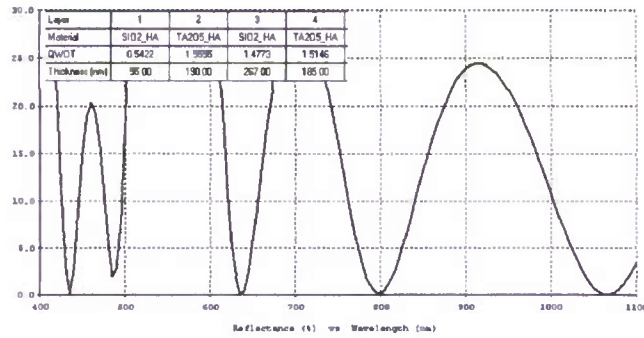
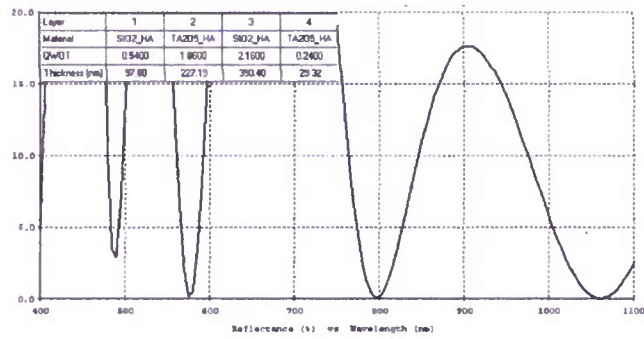
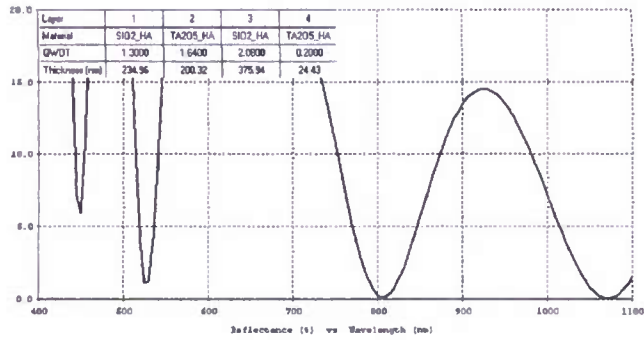
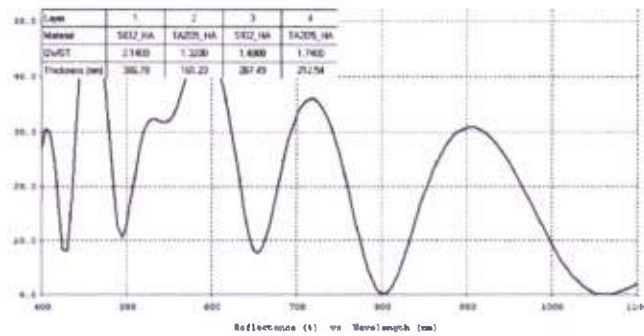


Figure 34. Four layer AR designs for vanadate crystal. (b)top (c)middle (d)bottom



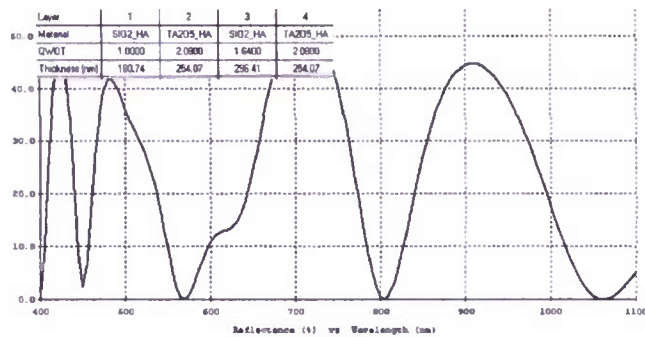


Figure 35. Four layer AR designs for vanadate crystal. (e) Top (f)Bottom

After comprehensive evaluation, the optimal coating design was still the four-layer one we mentioned in figure 33.

2.3 Coating for phosphate glass

2.3.1 Properties of phosphate glass plate

Phosphate glass is a class of optical glasses that are useful for solid state lasers.

2.3.2 AR coating design for phosphate glass plate (AR@808nm(<1%) and 1064nm(<0.1%))

The coating design target is still set as AR@808nm(<1%) and 1064nm(<0.1%), where the pumping wave length is at 808nm and the generated laser wave length is at 1064nm. Again, we will do a thorough search of all possible designs which meet the above AR specification, listing from simple to complex. The maximum total coating thickness is set as around 2um and the maximum coating layers as 5. For each coating design, we will show the coating structure and the resulted reflectance performance. The pro and con of each design will also be briefly introduced.

a. Two layer design

As shown in figure 37, this simplest coating structure can well satisfy the AR requirement at 1064nm. However, the limit of this design is also obvious. First, the AR value at 808nm can barely reach about 1%. If considering the error of layer thickness control, the AR performance at 808nm can only reach 2%. Secondly, the average AR performance in the band between 808nm and 1064nm is almost 4%, which will make a poor coating error tolerance.

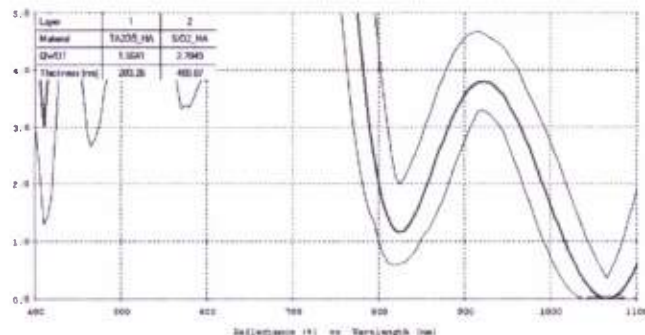


Figure 37. AR design of 2-layer structure.

b. Four layer AR design

In this case, totally 7 practical designs were identified. These designs were listed in the following figures (38-1 to 38-7) according to their AR performance. Usually, better AR performance (average reflectance between 800nm and 1064nm) comes together with thinner totally coating thickness.

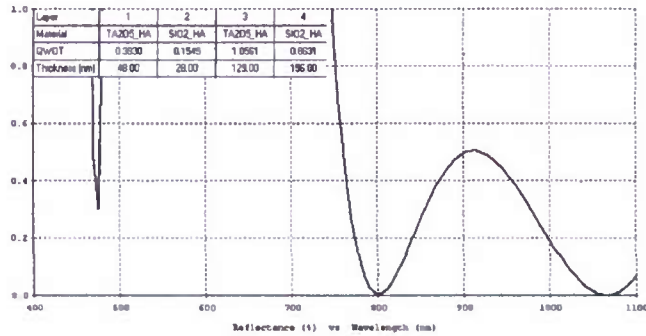


Figure 38-1.

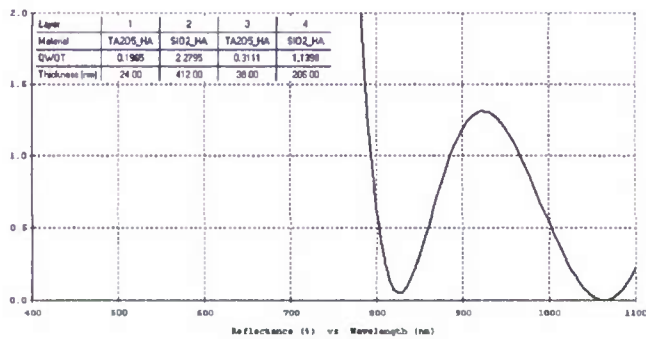


Figure 38-2.

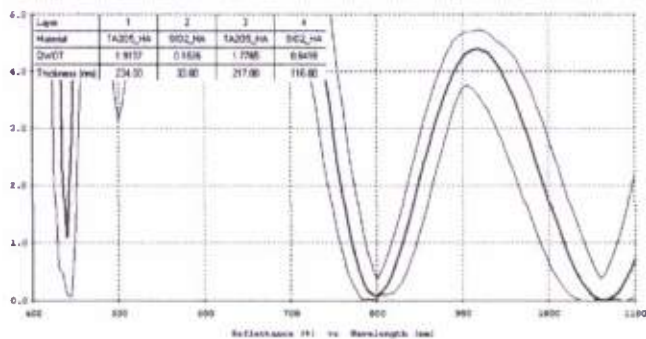


Figure 38-3.

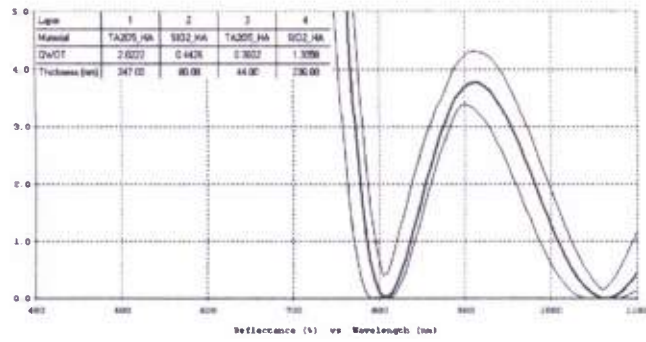


Figure 38-4.

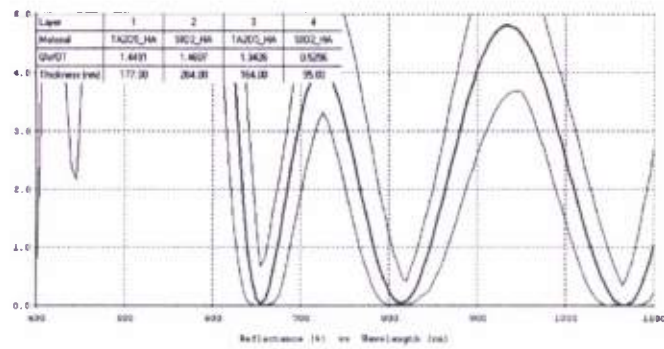


Figure 38-5.

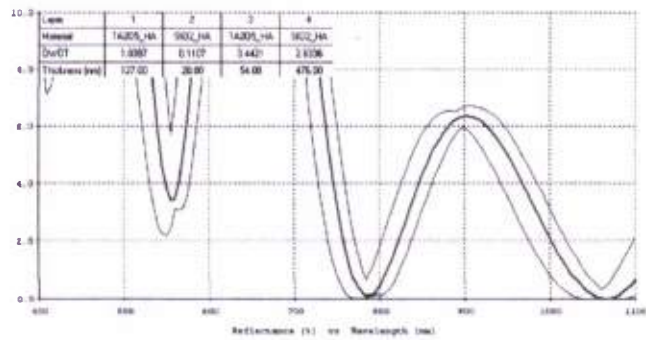


Figure 38-6.

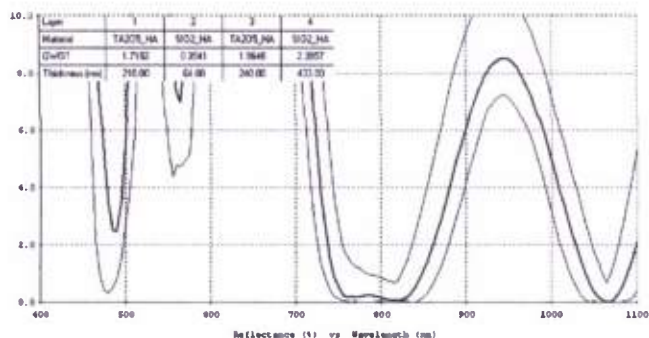
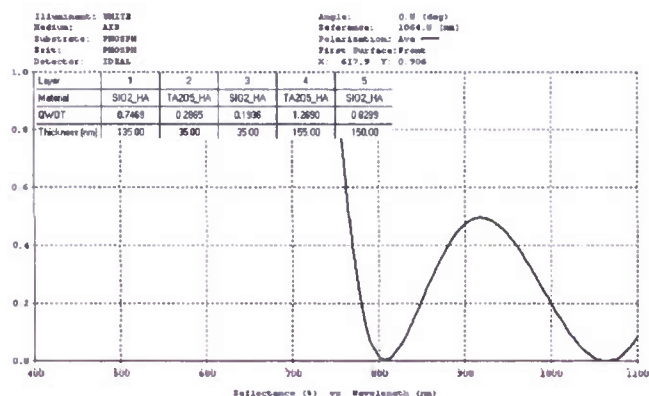


Figure 38-7.

Among the above 7 designs, it is clear that 38-1 is the best AR coating design, which has the thinnest total coating thickness and lowest average reflectance between 800nm and 1064nm. However, phosphate coating was well known for its poor adhesion, which may be related with the coating material of the first layer. In the design 38-7, the first layer was high index material Ta_2O_5 , whose material properties different a lot with low refractive index phosphate substrate. Therefore, it may lead to poor coating adhesion.

To solve this problem, an additional SiO_2 layer was inserted in design 38-7 as the first coating layer. Because of the very close refractive index value between phosphate and SiO_2 , the structure of the remaining four layers was almost the same. After optimization, the following 5-layer AR design (figure 39) was achieved with SiO_2 as the contact layer. Compared with the 38-1 design, another advantage of this design lies in its thicker first layer, which is 135nm instead of 35nm. The thicker first layer typically was stronger mechanically. Therefore, it can sustain higher coating stress.

Figure 39. Optimized 5-layer AR coating design based on b-1 structure, with SiO_2 as first layer.

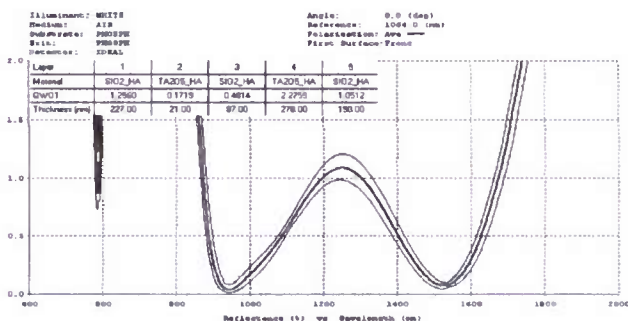
2.3.3 Double band AR coating design on phosphate glass

As shown in figure 40, another project of double band (900-1000nm & 1500-1600nm) AR coating design on phosphate glass was performed. Compared with the first project of only two target wavelength points, this project is more difficult because of the target of double wavelength bands.

Coating Specs.							
# Surf	Side/Face Dimension (mm)	□1 (nm)	Coating	AOI (Degree)	□2 (nm)	Coating	AOI (Degree)
BOTH ends	2.5 x 30mm	900-1000	R<0.2 %	0	1500-1600	R<0.2%	0

Figure 40. Double band (900-1000nm & 1500-1600nm) AR specification on phosphate glass.

Totally, 4 designs of 5-layer, 7-layer, 9-layer and 11-layer were identified and listed as the following. These designs are listed in the following figures 41, 42, 43, 44. Generally, thicker total coating and more coating layers will lead to steeper “side wall” of the target wavelength bands in the reflectance spectrum, which also means larger error tolerance of the design.



Phosphate

225nm SiO₂ / 21nm Ta₂O₅ / 86nm SiO₂ / 271nm Ta₂O₅ / 188nm SiO₂

Air

Figure 41. AR coating design of 5-layer structure and 800um total thickness(red figure is after annealing compensation)

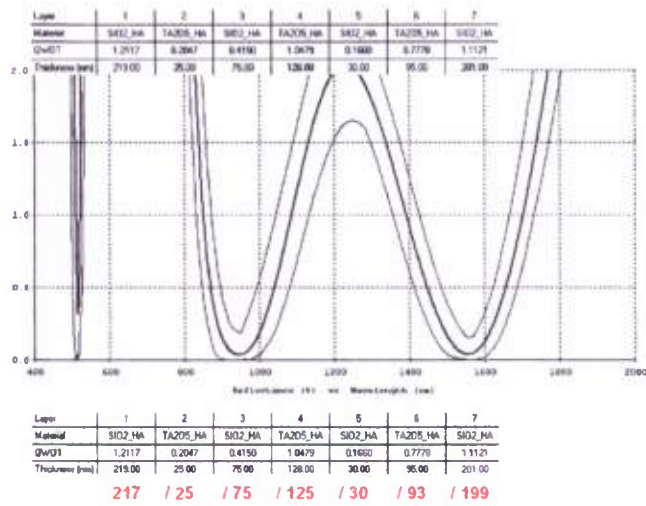


Figure 42. AR coating design of 7-layer structure (red figure is after annealing compensation)

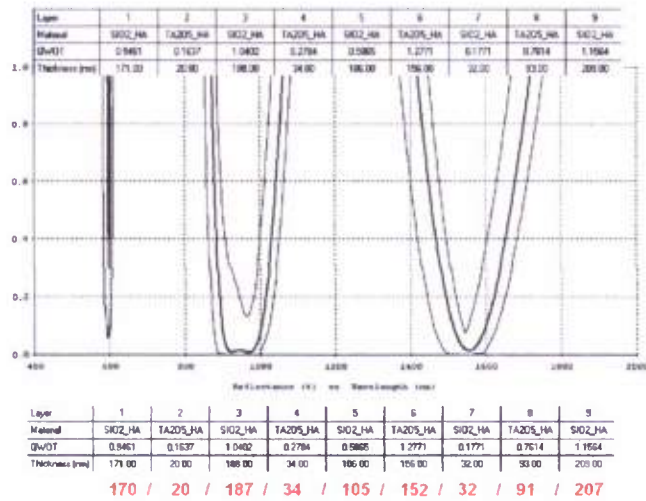


Figure 43. AR coating design of 9-layer structure (red figure is after annealing compensation)

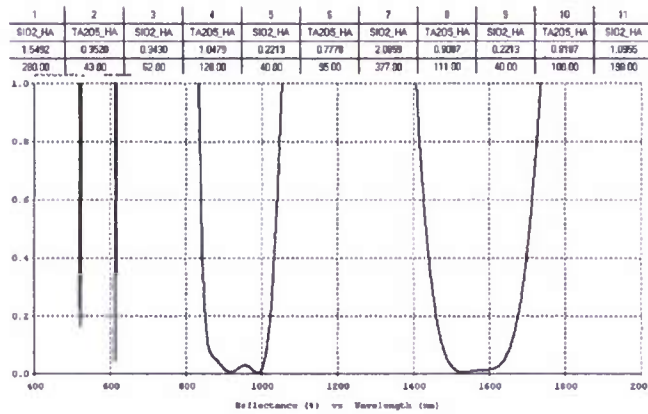


Figure 44. AR coating design of 11-layer structure with total thickness 1.5μm.

2.3.4 Test of coating samples

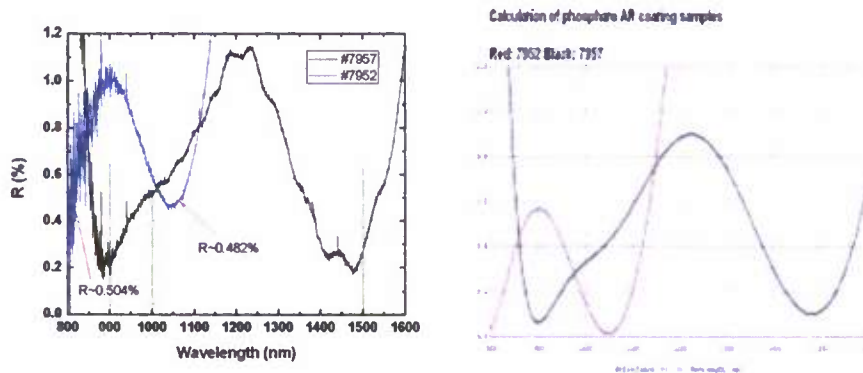


Figure 45. Comparison of theoretical calculation and spectrophotometer measurement.

2.4. Coating design for YLF crystal

2.4.1 Properties of YLF crystal

Neodymium-doped Yttrium Lithium Fluoride (Nd:LiYF₄, or Nd:YLF) crystal is an attractive alternative to the common YAG host for near IR operation. The combination of larger fluorescence line width (shown as Figure 46), long upper-state lifetime (485μs), naturally polarized oscillation and weak thermal lensing (19 times lower than that of YAG) makes Nd:YLF an excellent material for CW, mode-locked operation. 1.053μm output of Nd:YLF matches gain curves of Nd:Glass.

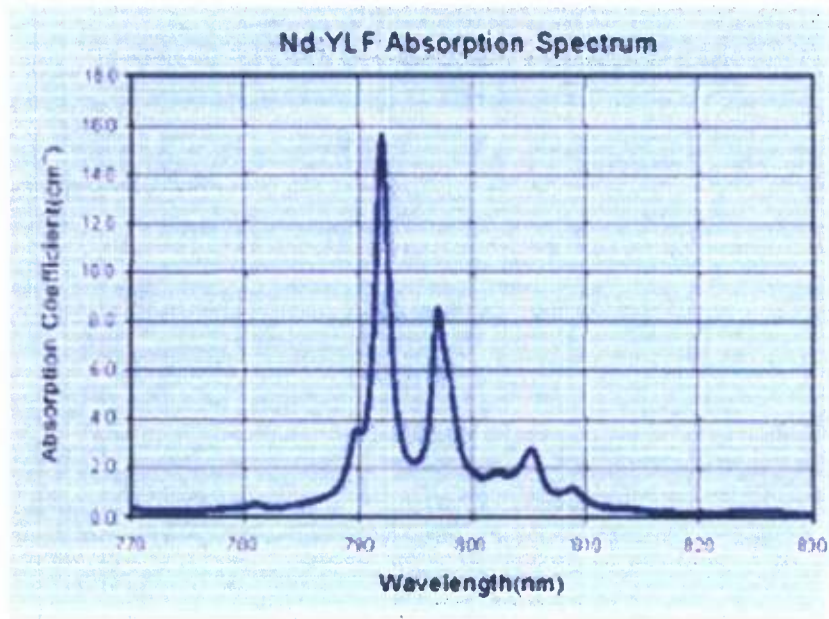


Figure 46. Absorption spectrum of Nd:YLF crystal

The refractive index values of the YLF crystal can be found in the figure 47 and 48.

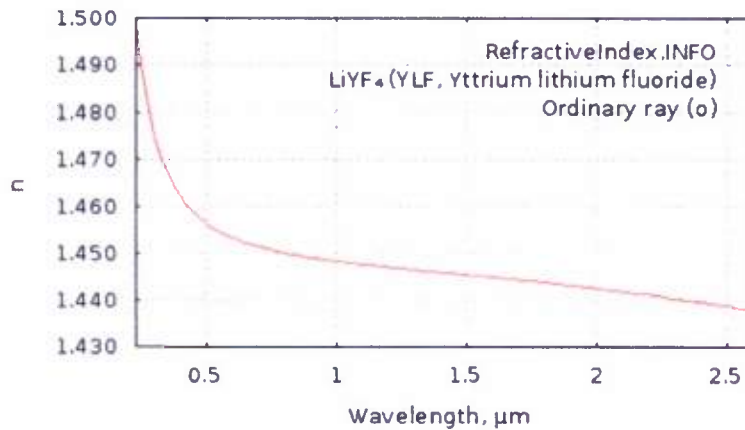


Figure 47. Refractive index curve under ordinary ray (o) with formula $n^2 = C_1 + C_2\lambda^2/(\lambda^2 - C_3) + C_4\lambda^2/(\lambda^2 - C_5)$, here $C_1 = 1.38757$; $C_2 = 0.70757$; $C_3 = 0.00931$; $C_4 = 0.18849$; $C_5 = 50.99741$.

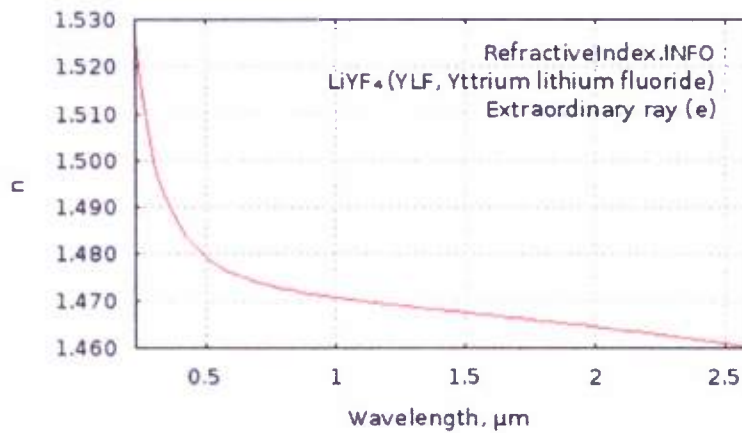


Figure 48. Refractive index curve under extraordinary ray (e) with formula $n^2 = C_1 + C_2\lambda^2/(\lambda^2 - C_3) + C_4\lambda^2/(\lambda^2 - C_5)$, here $C_1 = 1.31021$; $C_2 = 0.84903$; $C_3 = 0.00876$; $C_4 = 0.53607$; $C_5 = 134.9566$.

2.4.2 AR coating design for YLF crystal (AR@808nm(<1%) and 1064nm(<0.1%))

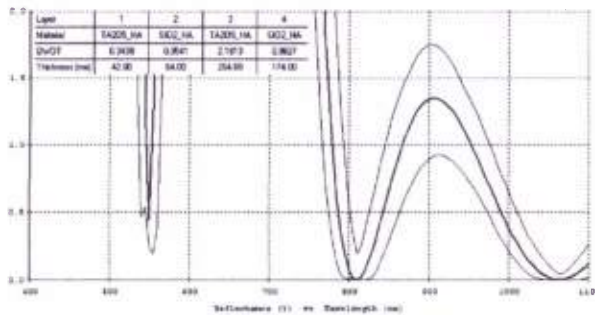


Figure 49. Optimized 4-layer design with total thickness around 500nm.

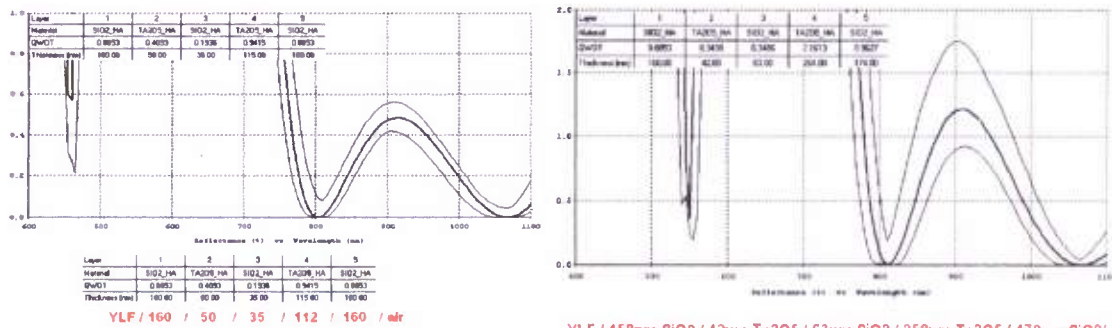
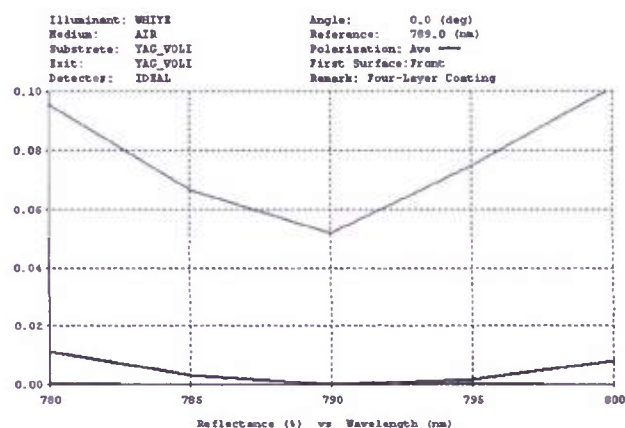


Figure 50. Two 5-layer designs.

2.5 Coating design for Tm:YAG laser

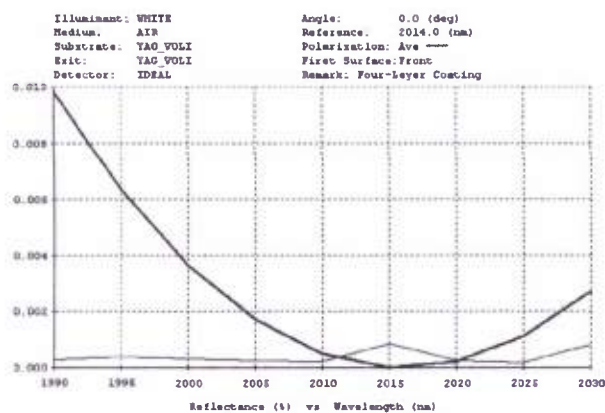
Shown in figure 51, coating designs for various coating types used in the Tm:YAG laser have been performed. The primary coating solution, analysis, and suggestion are listed in the following. All the coatings are on 12 mm × 12 mm × 0.5 mm YAG substrate.

2.5.1 AR coating



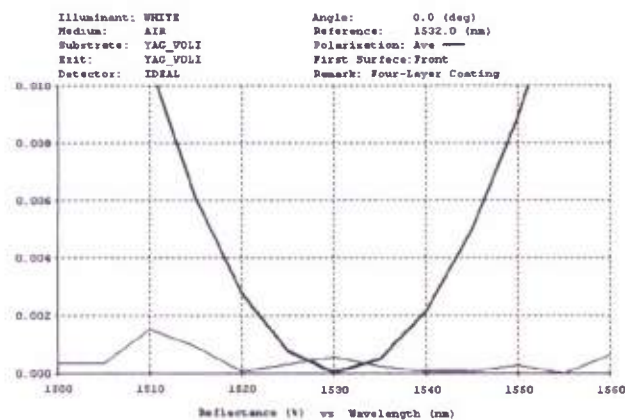
Layer	1	2
Material	TA205_V	SiO2_V
QWOT	0.3852	1.1623
Thickness (nm)	34.00	155.00

Figure 51-1. AR (R<0.1%) @ 785 nm to 793 nm.

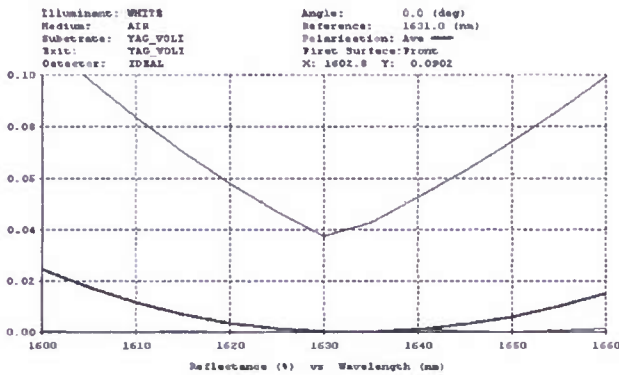


Layer	1	2
Material	TA205_V	SiO2_V
QWOT	0.4006	1.1554
Thickness (nm)	92.00	395.00

Figure 51-2. AR (R<0.1%) @ 2014 nm.



Layer	1	2
Material	TA205_V	SiO2_V
QWOT	0.3960	1.1543
Thickness (nm)	69.00	300.00

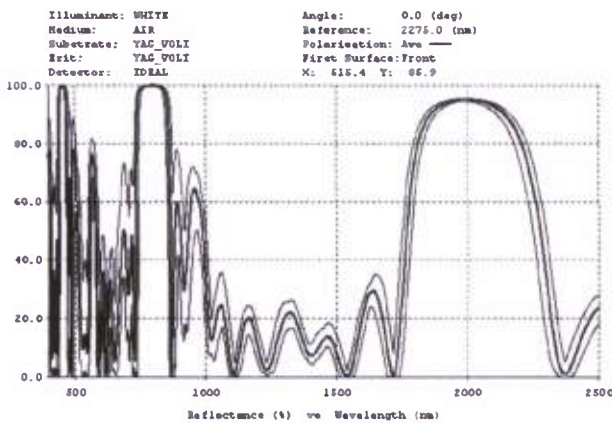
Figure 51-3. AR ($R < 0.1\%$) @ 1531 nm

Layer	1	2
Material	TA205_V	SiO2_V
QWOT	0.3986	1.1563
Thickness (nm)	74.00	320.00

Figure 51-4. AR ($R < 0.1\%$) @ 1617nm to 1645 nm.

All above AR coatings are for either single wavelength or narrow wavelength band. Therefore, typical two-layer coating design with total thickness less than 500nm can reach the target.

2.5.2 HR coating in near-IR band

Figure 51-5. $R > 99\%$ @ 785 to 793 nm; $R = 95\%$ @ 2014 nm.

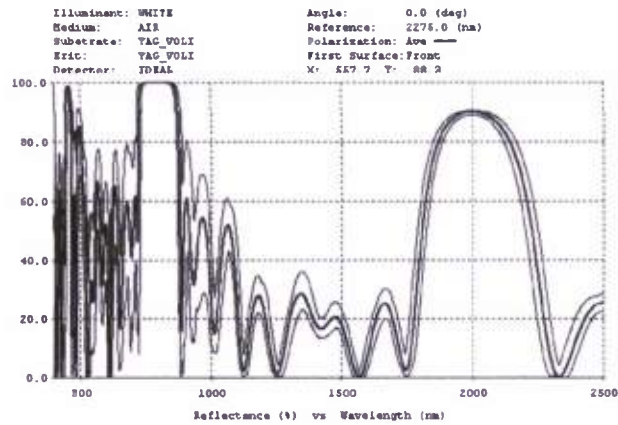


Figure 51-6. $R > 99\%$ @ 785 to 793 nm; $R = 90\%$ @ 2014 nm.

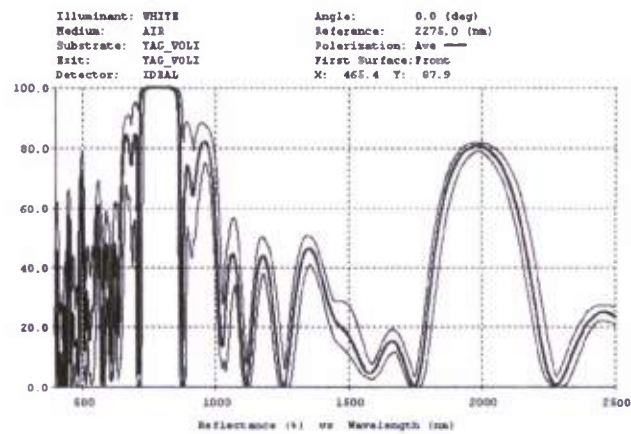


Figure 51-7. $R > 99\%$ @ 785 to 793 nm; $R = 80\%$ @ 2014 nm.

As the working wavelength is in the near IR band, the above three HR coatings can be realized with a 25-layer coating design, whose total thickness is around 3.5 μm .

2.5.3 HR coating in the IR band

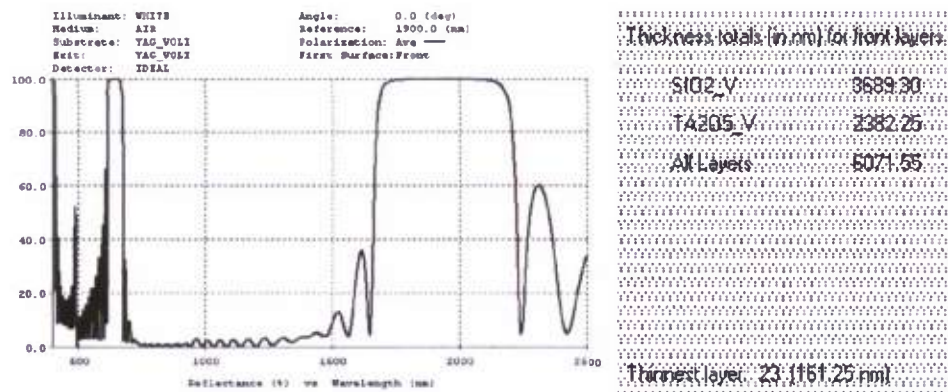


Figure 51-8. $T > 95\%$ (best effort for $T > 99\%$) @ 785 nm to 793 nm; $R > 99.9\%$ @ 2014 nm.

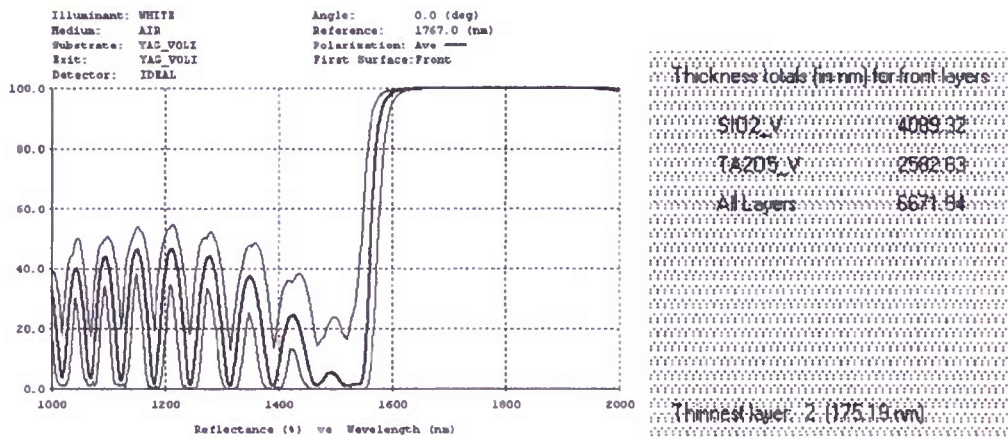


Figure 51-9. T>95% (best effort for T>99%) @ 1531 nm; R>99.9% @ 1617nm to 1645 nm.

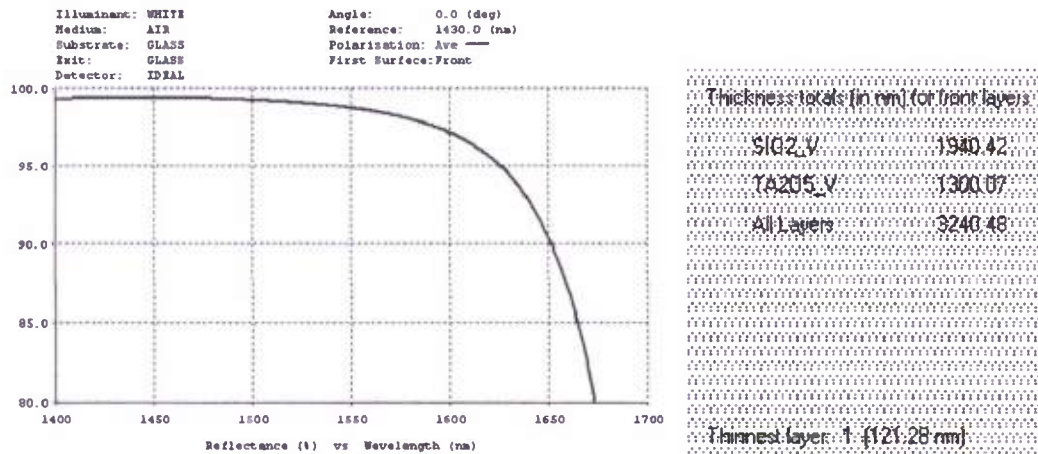


Figure 51-10. R>99% @ 1531 nm; R=95% @ 1617 to 1645 nm;

Because of the close distribution between the AR band and HR band, which is no more than 100nm, the coating design for 9 and 10 has posed certain challenge. Even though the theoretical designs for the above HR coating types can still be successfully realized, their production may prove to be difficult with our current coating equipment. The reason lies in the total thickness of over 6μm as compared with typical 2μm total coating thickness. Considering such thick coating, the stress on the coating will be tremendous. Without a proper stress releasing step, the achieved coating may have a great chance of cracking or delaminating.

2.6 Coating designs for Tm:YAG laser

The challenging coatings for the Tm:YAG laser have been successfully designed. The following figures 52-54 show the coating specifications and the relative designs.

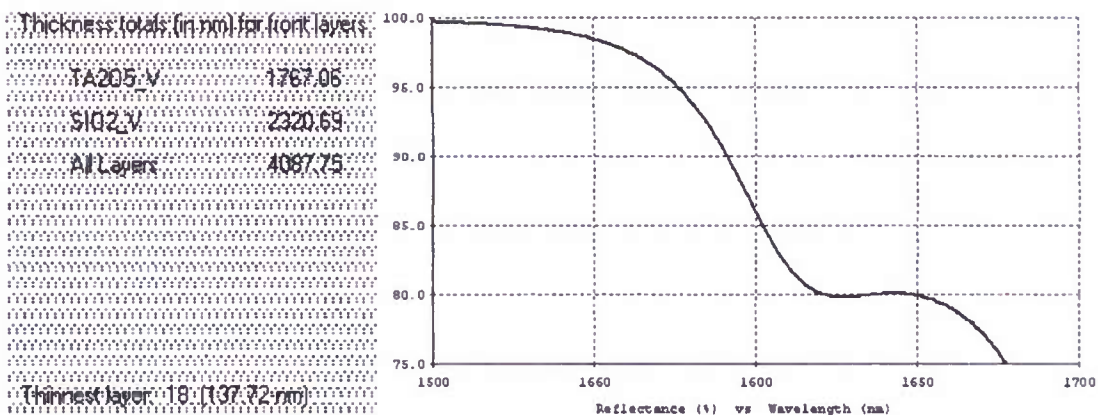


Figure 52. Coating design for YAG: $R > 99\%$ @ 1531 nm; $R = 80\%$ @ 1617 to 1645 nm ($\pm 1\%$)

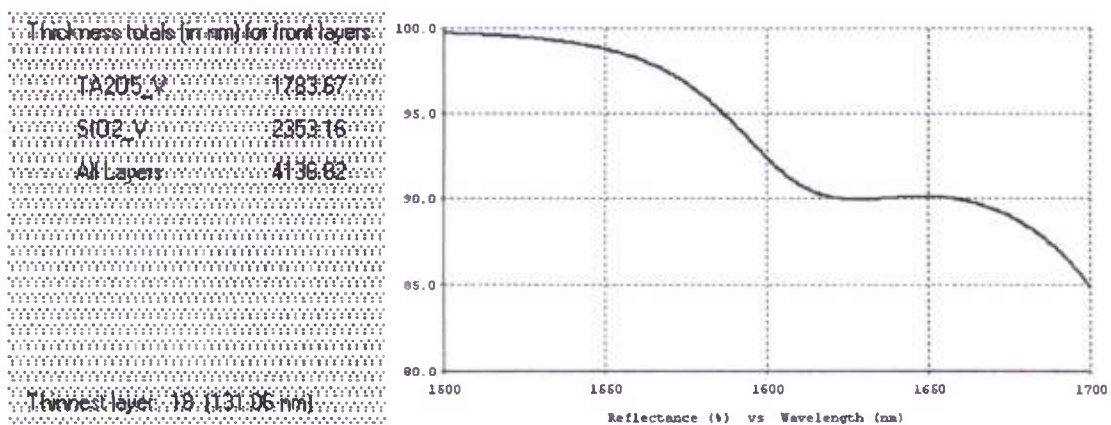


Figure 53. Coating design for YAG: $R > 99\%$ @ 1531 nm; $R = 90\%$ @ 1617 to 1645 nm ($\pm 1\%$)

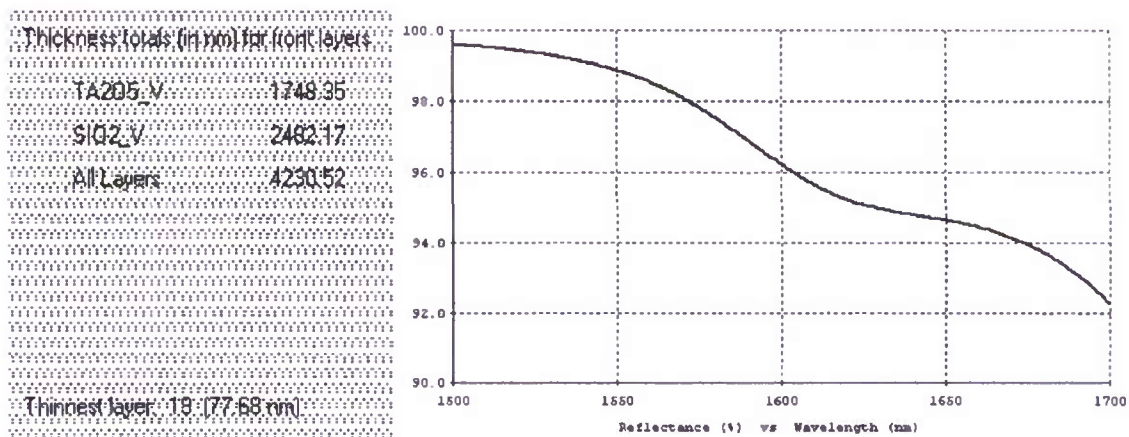


Figure 54. Coating design for YAG: $R > 99\%$ @ 1531 nm; $R = 95\%$ @ 1617 to 1645 nm ($\pm 1\%$)

As mentioned above, such coatings feature a “shoulder” very close to the flat “top” in the reflectance curve. Illustrated in figure 55, the design starts with $(HL)^{10}H$ structure. Among these 21 layers, the key lies in the two layers of 18th and 19th. After optimizing just these two layers, we can successfully realize all above coating designs.

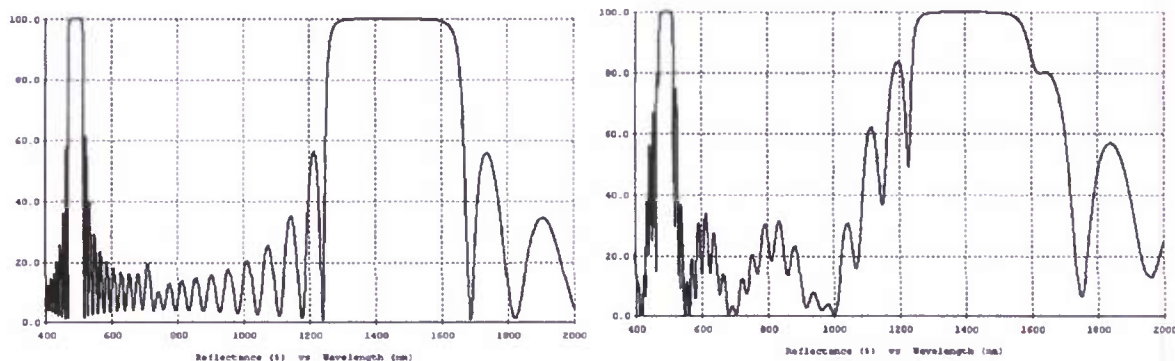


Figure 55. Reflectance curves of Left: initial $((HL)^{10}L)$ structure and Right: final design.

2.7 AR coating designs for Hyrax laser

AR coatings for Hyrax laser have also been designed and evaluated. The substrates are fused silica and CaF_2 , and the working wavelengths are 1907nm and 2097nm separately. The optical index values of the substrates are shown in figure 56 and 57.

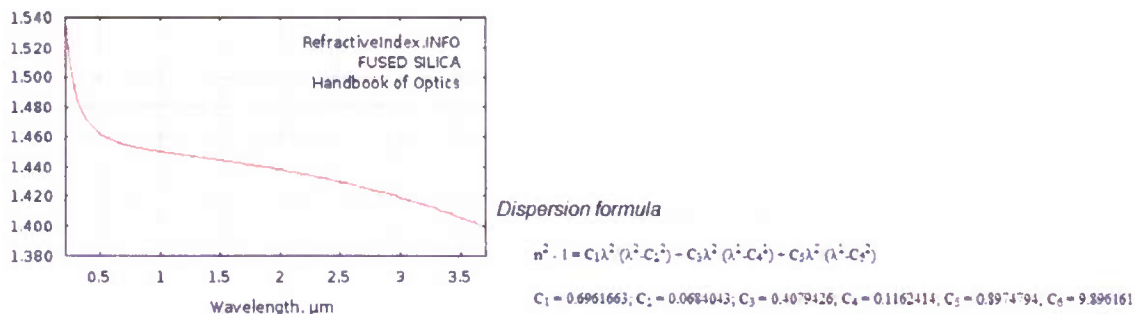


Figure 56. Refractive index curve of fused silica.

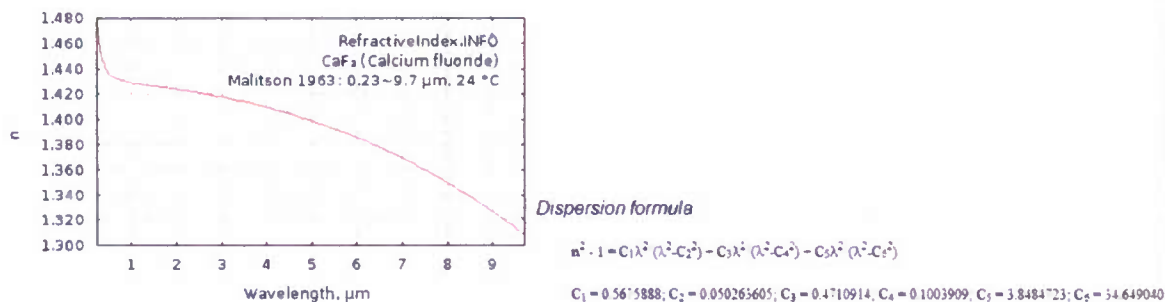


Figure 57. Refractive index curve of CaF_2 .

Even though the working wavelength is close to 2 μ m, the coating materials of SiO₂ and Ta₂O₅ can still satisfy the requirements in figure 58, 59. The single wavelength AR coating can be easily realized by double layer coating structure, so called V-shape coating. The total thickness is around 0.5 μ m, almost 4 times thicker than that working in the visual band. However, such a coating is not difficult to manufacture. If the coating adhesion turns out to be an issue, an additional layer of 0.1 μ m SiO₂ may be inserted between the Ta₂O₅ and substrate. This additional layer will work as a matching layer to enhance the coating adhesion.

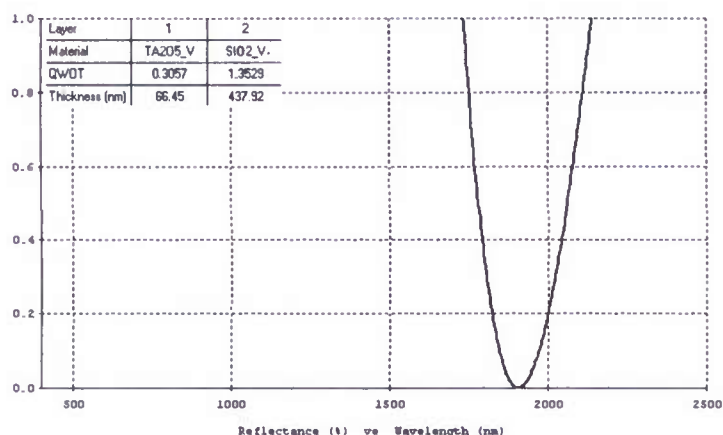


Figure 58. Coating design for Fused Silica: T>99.9% at 1907 nm, UV fused silica substrate lens.

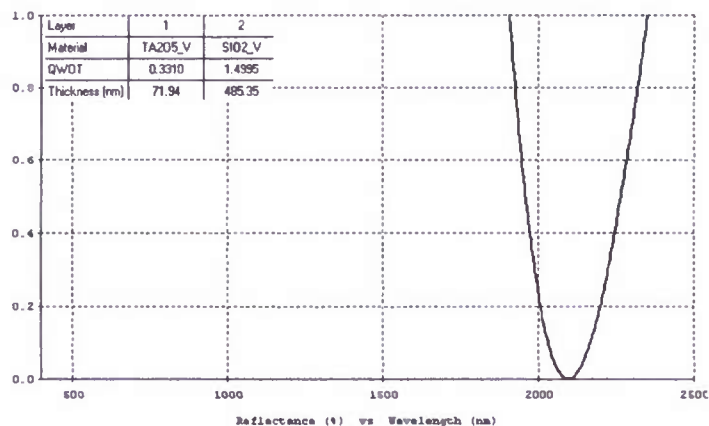


Figure 59. Coating design for CaF₂: T>99.9% at 2097 nm, CaF₂ lens and window

2.8. Stress evaluation of the 0.5 μ m AR coating on 350 μ m silicon wafer

To evaluate the coating stress, comparison of the substrate curvature before and after the coating has been shown in figure 60.

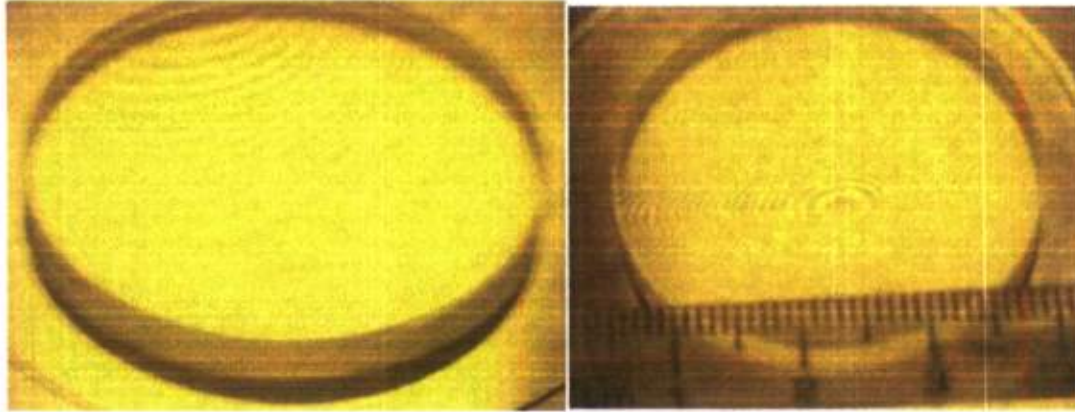


Figure 60. Comparison of the substrate curvature before and after the coating. Left) Initial interference pattern before coating. Right) interference pattern after coating. A high flatness glass plate was put on the 2'' silicon wafer whose thickness is 350um. After coating of 4-layer AR, whose thickness was around 0.5um, the interference pattern has changed significantly.

The light used was sodium lamp 0.589um yellow light. Roughly $m=20$ lines in $R_m=20\text{mm}$ from center to outside. According to the law of Newton's ring, curvature radius can be calculated as $R_m^2/m\lambda$ or 33m.

The intrinsic stress of the coating can be calculated as

$$\sigma_f = \frac{1}{6} \frac{E_s}{(1 - \nu_s)} \frac{t_s^2}{t_f} \left(\frac{1}{r_{f+s}} - \frac{1}{r_s} \right)$$

Here, E_s is young's modulus value for silicon plate as 170GPa, ν_s is Poisson's ratio of silicon as 0.064, t_s is the thickness of substrate as 350um, and t_f is the thickness of film as 0.5um, $r_{(f+s)}$ is the curvature radius after coating as 33m. We assume r_s of initial substrate curvature as 0.

The result is 225MPa, which is a pretty reasonable value. Typical data from published paper was between 300 to 400 MPa for a thicker coating.

2.9 Effects of post annealing

It is well known that the post annealing was effective in reducing the stress and the light absorption of the coating. Our annealing was performed with a hot plate. In this case, there is a 50°C difference at the plate surface compared with the set point. Considering the optimal annealing temperature between 350°C and 400°C, annealing set point of the hot plate should be 450°C. The time period was set as 3.5h. After annealing, key parameters such as thickness, index value, absorption will be investigated in detail. Such information will be very important in optimizing the AR coating design.

2.9.1 Index and thickness change after annealing

The following figures 61-66 show the index and coating thickness change of three runs after annealing. As we found that the SiO_2 coating was pretty stable in both thickness and index value, while the Ta_2O_5 coating showed a 3% thickness increase and 1% refractive index drop.

RUN 1.

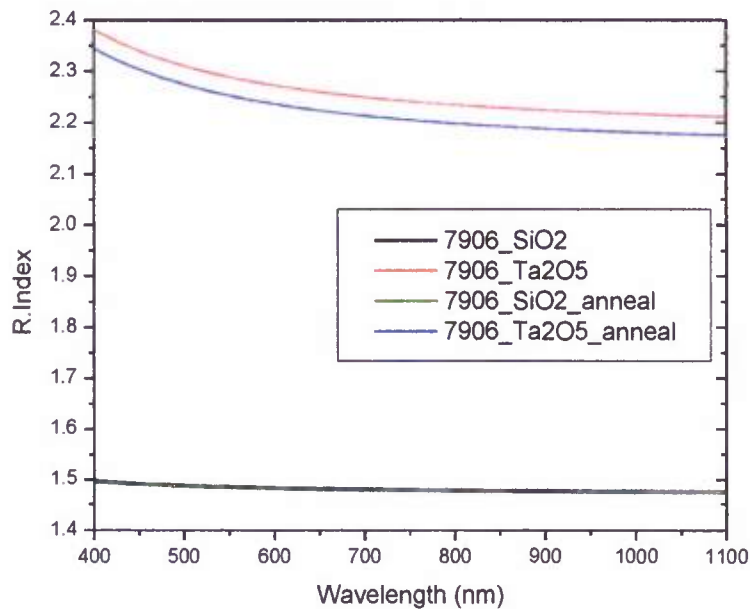


Figure 61. Reflective index curve shift before and after annealing. (RUN1)

Sample 1	Initial (nm)	Annealing (nm)	Error (%)
SiO2	186	188	+1.1
Ta2O5	276	285	+3.3
SiO2	44	44	+0
Ta2O5	60	62	+3.3

Sample 2	Initial (nm)	Annealing (nm)	Error (%)
SiO2	158	160	+1.3
Ta2O5	252	259	+2.8
SiO2	37	37.5	+1.3
Ta2O5	55.5	57	+2.7

Figure 62. Coating thickness change of the two samples in RUN1 before and after annealing

Run 2.

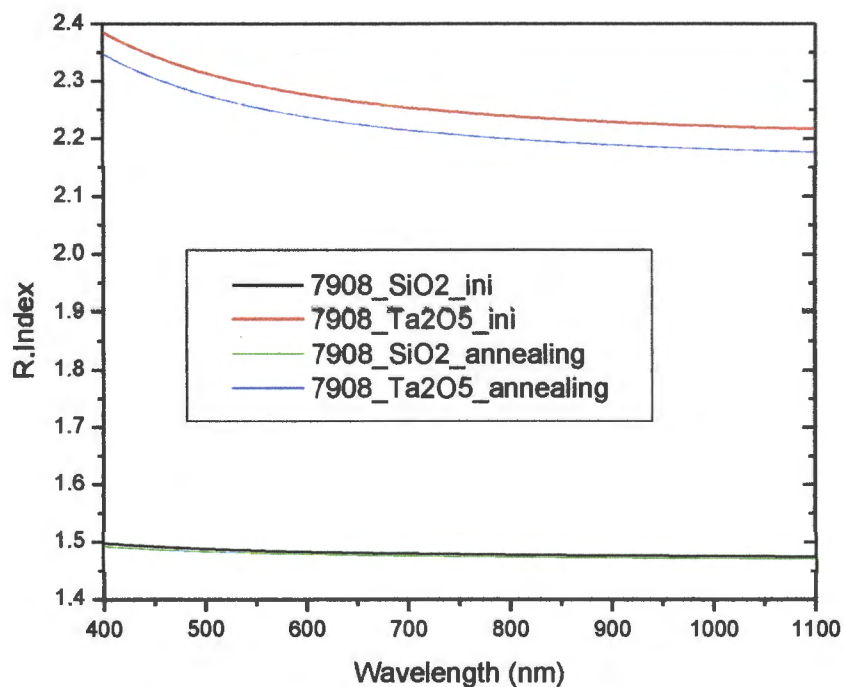


Figure 63. Reflective index curve shift before and after annealing. (RUN2)

Sample 1	Initial (nm)	Annealing (nm)	Error (%)
SiO2	161	162	+0.6
Ta2O5	257	264.3	+2.8
SiO2	37	37.7	+2
Ta2O5	55	56.2	+2

Sample 2	Initial (nm)	Annealing (nm)	Error (%)
SiO2	189.3	192.3	+1.6
Ta2O5	279	287.5	+3
SiO2	43.5	44	+1
Ta2O5	60	61.6	+2.6

Figure 64. Coating thickness change of the two samples in RUN2 before and after annealing

Run 3.

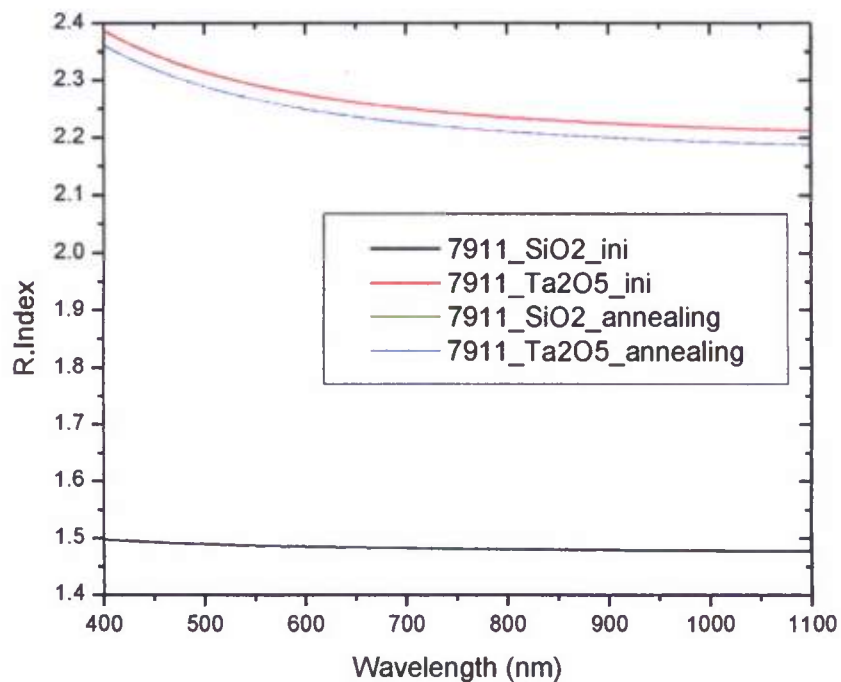


Figure 65. Reflective index curve shift before and after annealing. (RUN3)

Sample 1	Initial (nm)	Annealing (nm)	Error (%)
SiO2	155	156	+0.6
Ta2O5	245.3	252	+2.7
SiO2	22.3	22.1	+0

Sample 2	Initial (nm)	Annealing (nm)	Error (%)
SiO2	183.4	184	+0.3
Ta2O5	271	278	+2.6
SiO2	25.6	26.1	+2

Figure 66. Coating thickness change of the two samples in RUN3 before and after annealing

The above thickness and index value change after annealing play an important role in coating optimization. Its effects can be manifested in the following figure 67. Without appropriate compensation, the performance of the final coating may significantly shift away from the initial design.

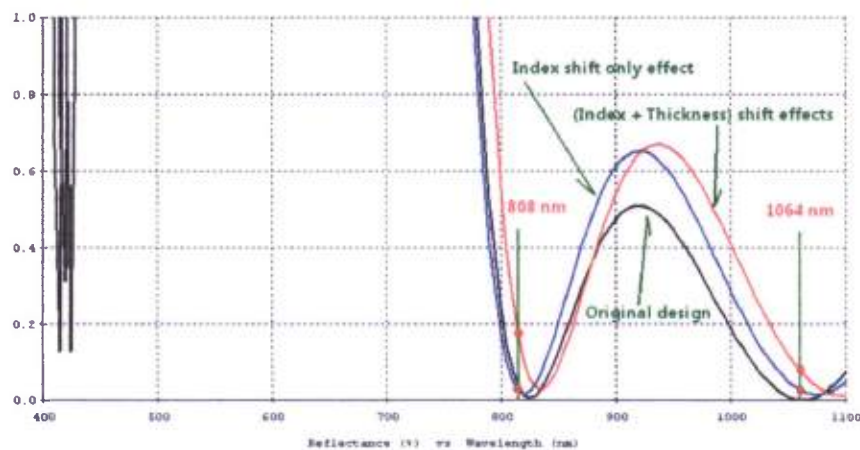


Figure 67. Annealing effects of index curve and coating layer thickness to the coating design

2.9.2 Light absorption of the coating material after annealing

While the SiO_2 coating material shows very limited light absorption, the Ta_2O_5 coating material has much stronger light absorption. And the annealing can effectively reduce such absorption 50% or even more. The following figure shows the effect of Ta_2O_5 absorption drop after annealing and its influence to the coating performance. All these factors should be considered and compensated properly to optimize the coating design, as illustrated in figure 68.

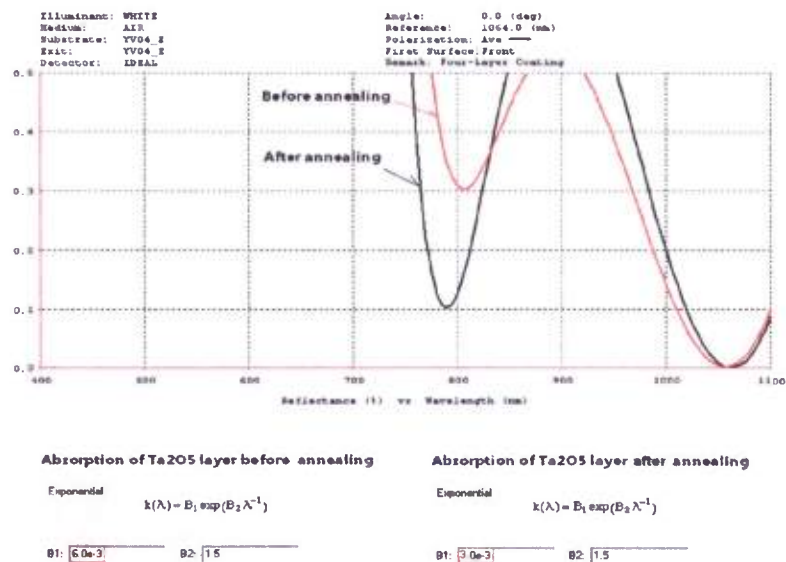


Figure 68. Annealing effect of Ta_2O_5 layer light absorption to the coating design

2.10. Metal sputtering work

2.10.1 Sputtering test on slides

Metal sputtering tests of different materials have been performed on the Denton desktop IV. The slide of 0.3mm thickness was chosen as the substrate. Materials tested are Au, Cr, W, Ti, Fe, Al, Ni. Typical coating process always starts with plasma cleaning of around 2 mins, and the formal sputtering may last 5 to 30 mins. The sputtering process is generally set as 5-10mbar of chamber pressure, 50% - 80% of DC voltage range. Finally, the surface profiler and ellipsometer are used to analyze the coating properties such as thickness, film density, refractive index, absorption coefficient.

Shown in figure 69, all sputtering samples show shiny metal color, good uniformity, and high reflectivity. Because of the strong light reflection, the photos may not reflect the real quality of the coating sample. Tapes were used either as masks during sputtering or as tools to remove backside reflection during ellipsometer measurement.

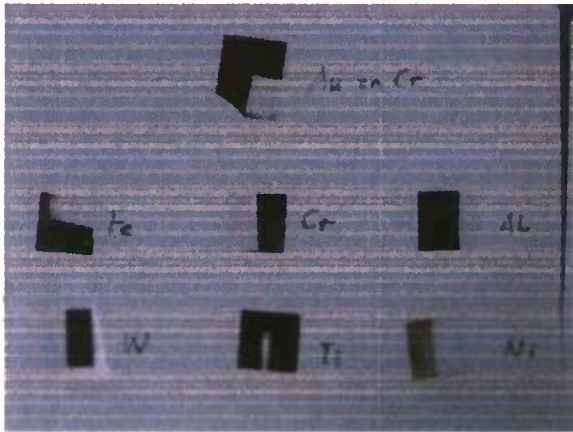


Figure 69. Metal coating samples from Denton Desktop IV sputtering system.

The ellipsometer measurement results of the above samples are listed in figure 70. The obtained refractive index and distinguish coefficient are listed together with that of the bulk material. Some materials like Au are easier to sputter. And, the sputtered coating is very close to that of bulk material. Generally, the sputtered coating is less dense than the bulk material, which leads to lower value of n and k .

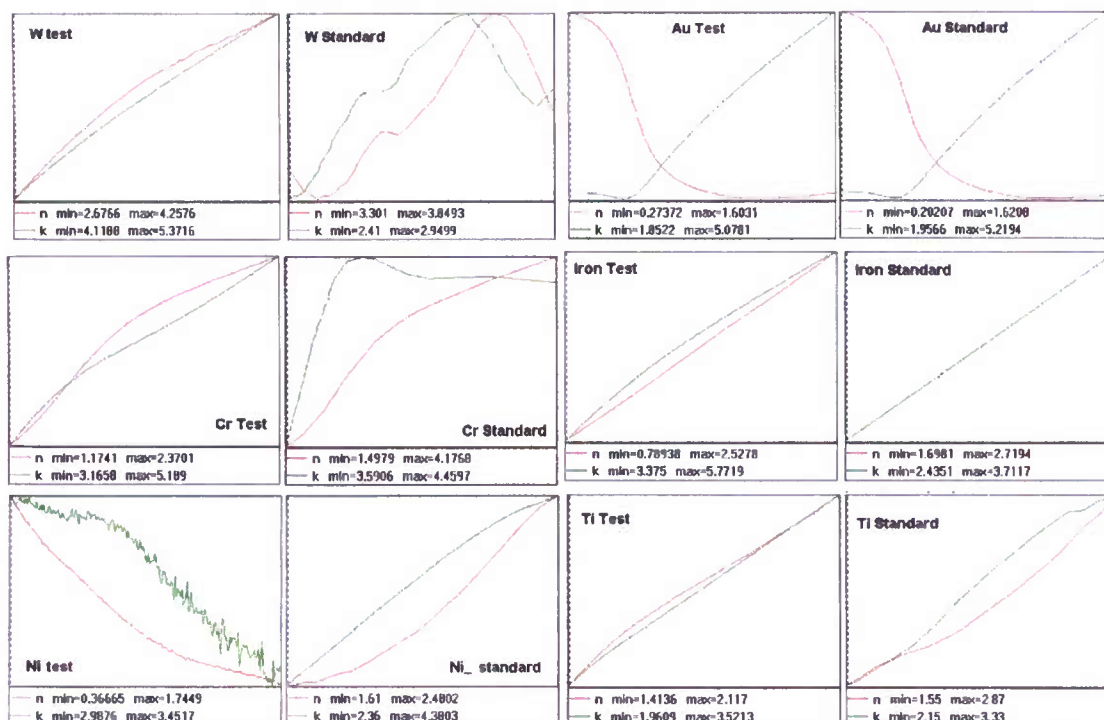


Figure 70. Ellipsometer measurement results of metal sputtering samples, compared with bulk material.

As our relatively small sputtering system is DC magnetron style, the most difficult sputtering materials are found to be ferromagnetic materials like Iron or Ni. First, the magnetic force between the ferromagnetic target and the magnetron makes it difficult to strike the plasma at low chamber pressure. Secondly, the sputtering efficiency is very low, and the target will be easily poisoned. As a result, the obtained coating is often semi-transparent and of low deposition rate. Based on the above analysis, the possible solutions are a) Enhanced magnetron. b) Thinner target. c) Doped target to reduce magnetic force.

2.10.2 Sputtering test on YAG crystal

A metal coating of Au/Cr has been successfully sputtered on the grinded YAG crystal. The process parameters were set as 5mTorr in pressure, 5 min in time, current around 50mA for Au and 30ma for Cr. The final coating thickness was 60nm for Au and 15nm for Cr. As shown in figure 71, the coating quality is pretty good.

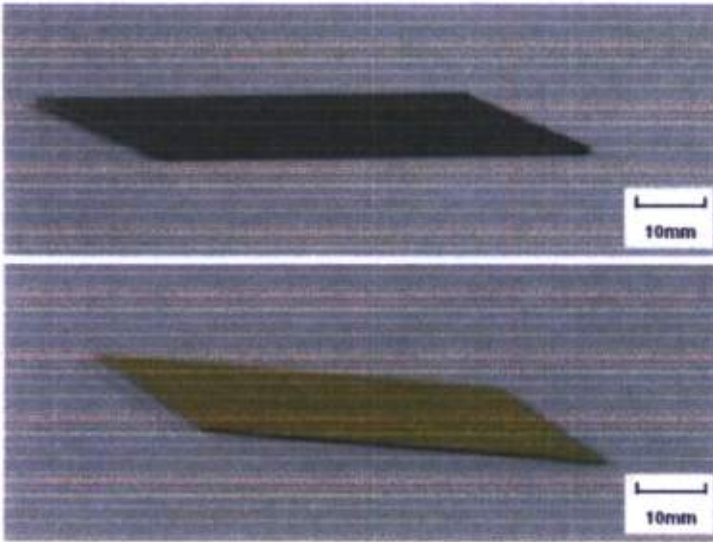


Figure 71. Au/Cr metal coating on YAG crystal. Top: before sputtering, Bottom: after sputtering.

Final Report for Contract # W911NF-07-2-0072

Accounting of all Federal funds expended during the term of the Agreement

Invoice #	Date		Invoice Amount	Total Amount Invoiced
Invoice 33	11/8/2010	33	\$152,510	\$152,510
Invoice 34	12/3/2010	34	\$203,248	\$355,758
Invoice 35	1/14/2011	35	\$102,666	\$458,424
Invoice 37	2/26/2011	37	\$221,243	\$679,667
Invoice 38	4/12/2011	38	\$157,622	\$837,289
Invoice 39	5/24/2011	39	\$191,261	\$1,028,550
Invoice 40	6/28/2011	40	\$215,160	\$1,243,710
Invoice 41	7/23/2011	41	\$188,669	\$1,432,379
Invoice 42	8/23/2011	42	\$100,688	\$1,533,067
Invoice 43	9/19/2011	43	\$145,009	\$1,678,076
Invoice 44	11/28/2011	44	\$21,924	\$1,700,000



'FORMING STRONG BONDS'

Defense Technical Information Center
8725 John J. Kingman Road, Suite 944
Ft. Belvoir, VA 22060

November 28, 2011

RE: Contract No. W911NF-07-2-0072

To Whom It May Concern,

Please find enclosed one printed copy of the Final Report for Contract No. W911NF-07-2-0072. Please do not hesitate to contact me if you have any questions.

Best Regards,

Rachael L. Goodwin

Rachael L. Goodwin
Office Manager